

1 **Shallow Slow Earthquake Episodes Near the Trench Axis Off Costa Rica**

2

3 **Satoru Baba¹, Kazushige Obara¹, Shunsuke Takemura¹, Akiko Takeo¹, and Geoffrey A.**
4 **Abers²**

5 ¹Earthquake Research Institute, The University of Tokyo, Tokyo, Japan

6 ²Department of Earth and Atmospheric Sciences, Cornell University, Ithaca, New York, United
7 States of America

8

9 Corresponding author: Satoru Baba (babasatoru@eri.u-tokyo.ac.jp)

10

11 **Key Points:**

- 12 • Shallow very low frequency earthquakes and tremors are detected off Costa Rica near the
13 Middle America Trench
- 14 • Distribution of these slow earthquakes is separated from coseismic slip areas of tsunami
15 and large earthquakes
- 16 • Distribution and scaled energy of shallow slow earthquakes off Costa Rica are similar to
17 those in Nankai

18

19 **Abstract**

20 Slow earthquakes are mainly distributed in regions surrounding seismogenic zones
21 along the plate boundaries of subduction zones. In the Central American subduction zone, large
22 regular interplate earthquakes with magnitudes of 7–8 occur repeatedly around the Nicoya
23 Peninsula, in Costa Rica, and a tsunami earthquake occurred off Nicaragua, just north of Costa
24 Rica, in 1992. To clarify the spatial distribution of various slip behaviors at the plate boundary,
25 we detected and located very low frequency earthquakes (VLFs) around the Nicoya Peninsula
26 using a grid-search matched-filter technique with synthetic templates based on a regional three-
27 dimensional model. VLFs were active in September 2004 and August 2005, and most of the
28 VLFs were located near the trench axis at a depth range of 6–10 km, updip of the seismogenic
29 zone. The spatial distribution of VLFs complements the slip areas of large earthquakes and the
30 tsunami earthquake. Low frequency tremor signals were also found in high-frequency
31 seismogram envelopes within the same time windows as detected VLFs; thus, we also
32 investigated the energy rates of tremors accompanied by VLFs. The range of scaled energy,
33 which is the ratio of the seismic energy rate of a tremor to the seismic moment rate of
34 accompanying VLF, was 10^{-9} – 10^{-8} . The along-dip separation of shallow slow and large
35 earthquakes, the ranges of magnitude and source duration of VLFs, and energy rate of tremors
36 off Costa Rica are similar to those in shallow slow earthquakes in Nankai, which shares a similar
37 thermal structure along the shallow plate boundary.

38 **Plain language summary**

39 Slow earthquakes with slower rupture speeds compared to those of regular earthquakes
40 generally occur on the plate boundaries of subduction zones. We detected and located very low
41 frequency earthquakes (VLFs), which are a type of slow earthquake, off Costa Rica. The
42 VLFs occurred at a depth range of 6–10 km, and their distribution fills the gaps between slip
43 areas of tsunami and large regular earthquakes. The spatial separation of slow and large regular
44 earthquakes is also common to the Nankai subduction zone. Low frequency tremor signals,
45 which are also classified as slow earthquakes, are also found in seismograms at higher
46 frequencies within the same time windows of detected VLFs. We also estimated the ratio of
47 energy rates of tremors to moment rates of VLFs, which relates to the rupture process of
48 seismic phenomena. The ratio is 10^{-9} – 10^{-8} off Costa Rica, similar to that in shallow slow
49 earthquakes in the Nankai subduction zone.

50 **1. Introduction**

51 Slow earthquakes are mainly observed in regions surrounding seismogenic zones, which
52 are the areas that rupture in large regular earthquakes, along the plate boundaries of subduction
53 zones (e.g., Obara & Kato, 2016) or strike-slip faults (e.g., Nadeau & Dolenc, 2005; Wang &
54 Barbot, 2020). Various types of slow earthquakes, such as low frequency tremors (tectonic
55 tremors; e.g., Obara, 2002), low frequency earthquakes (LFEs; e.g., Shelly et al., 2006), very low
56 frequency earthquakes (VLFs; e.g., Obara & Ito, 2005), and slow slip events (SSEs; e.g.,
57 Dragert et al., 2001) have been observed in many subduction zones. Although these slow
58 earthquake phenomena occur without correlation in some cases (Hutchison, 2020; Hutchison &
59 Ghosh, 2016, 2019), they often correlate spatiotemporally, which is termed episodic tremor and
60 slip (ETS). ETSs were observed in deep Cascadia (e.g., Ghosh et al., 2015; Rogers & Dragert,
61 2003) and deep Nankai (e.g., Ito et al., 2007; Obara, 2011), for example. Recently, in the Nankai

62 subduction zone, pore fluid pressure changes have been observed during tremor and VLFE
63 activities and are considered to reflect shallow SSEs by offshore borehole observations (Araki et
64 al., 2017; Nakano et al., 2018). The hypocenters and focal mechanisms of slow earthquakes are
65 generally consistent with shear slip on the plate boundaries. VLFE episodes and SSEs occur in
66 almost identical source regions and their temporal changes of moment release are similar during
67 as ETS, therefore VLFE episodes are considered as proxies for SSEs (Ghosh et al., 2015; Ito et
68 al., 2007; Nakano et al., 2018; Yokota & Ishikawa, 2020). In summary, the distribution of slow
69 earthquakes is related to large earthquake slip areas, interplate coupling, or fluid distribution
70 (e.g., Baba et al., 2020b; Ghosh et al., 2015; Obara & Kato, 2016).

71 In the Central American subduction zone, the Cocos plate subducts beneath the
72 Caribbean plate at the Middle America Trench at a rate of approximately 80 mm/year (Figure 1b;
73 referred from NUVEL1A; DeMets et al., 1994). In this subduction zone, large thrust-type
74 earthquakes with a moment magnitude (M_w) of 7–8 occur with a recurrence interval of tens of
75 years around the Nicoya Peninsula, in Costa Rica (light blue areas in Figure 1a; Protti, 1995; Yue
76 et al., 2013). The coseismic slip areas of these large earthquakes are distributed at a depth range
77 of 10–35 km beneath the peninsula and off the coast. The latest large earthquake with M_w of 7.6
78 occurred on 5 September, 2012 (green contour lines in Figure 1a; Yue et al., 2013). In the
79 vicinity, a tsunami earthquake with M_w of 7.6 also occurred off Nicaragua, just north of Costa
80 Rica, on 2 September, 1992 (dark blue area in Figure 1a; Satake, 1994).

81 In addition to large regular and tsunami earthquakes, slow earthquakes also occur around
82 the Nicoya Peninsula. The Global Navigation Satellite System data revealed that SSEs with M_w
83 of 6.6–7.2 occur at intervals of 21.7 ± 2.6 months (Jiang et al., 2012; Xie et al., 2020). The large
84 slip area of the SSE in 2007 was separated into downdip and updip areas by the seismogenic slip
85 area (Jiang et al., 2012, 2017; Outerbridge et al., 2010). The spatiotemporal change in relation to
86 the 2012 M_w 7.6 earthquake was investigated by previous studies (Dixon et al., 2014; Voss et al.,
87 2017), and an SSE preceded the 2012 M_w 7.6 earthquake (Voss et al., 2018) in the almost same
88 area of the 2007 SSE, similar to both the slow slip before the 2011 Tohoku earthquake in Japan
89 (Ito et al., 2013; Kato et al., 2012) and the slow slip before the 2014 Iquique earthquake in Chile
90 (Kato & Nakagawa, 2014; Ruiz et al., 2017).

91 By using high-frequency (>1 Hz) seismograms, Brown et al. (2009) and Outerbridge et
92 al. (2010) located LFEs and tremors in 2007, respectively (Figure 1a). The tremors and LFEs
93 were located in almost the same area, downdip of the seismogenic zone. Although tremors and
94 LFEs were temporally correlated with the SSE, the location of tremors and LFEs were separated
95 from the large slip area of the 2007 SSE. On the other hand, Walter et al. (2011) located many
96 tremors in the offshore region from 2007 to 2009. Walter et al. (2013) also found that VLFs
97 appeared in seismograms in a frequency range of 0.02–0.05 Hz and were temporally correlated
98 with tremors in the time period of the 2008 SSE. Based on beamforming analysis, they estimated
99 the propagation direction and the propagation speed of VLFE signals and suggested that VLFs
100 also occurred in offshore areas. Due to the limitations of a conventional analysis, however,
101 epicenters of VLFs in offshore areas were not located. Therefore, the detailed spatial
102 distribution of slow earthquakes off Costa Rica is still not well understood.

103 The spatial variation of slow and large regular earthquakes can reflect the spatial
104 heterogeneity of the frictional conditions on the plate boundary (e.g., Baba et al., 2020b). To
105 clarify the spatial relationship between slow and large regular earthquake distribution around the
106 Nicoya Peninsula, an accurate spatial distribution of slow earthquakes is needed. Thus, we

107 detected VLFES around the Nicoya Peninsula using a temporary broadband seismic network
108 from August 2004 to January 2006 because signals of VLFES are less attenuated than those of
109 tremors and propagate longer distances. The method is based on the matched-filter technique.
110 Template waveforms from possible VLFES locations were evaluated by numerical simulations of
111 seismic wave propagation using a regional three-dimensional (3D) velocity structure model. In
112 addition, scaled energy is an informative parameter for the rupture process of seismic phenomena
113 (Kanamori & Rivera, 2006). By using high-frequency (2–8 Hz) seismograms, we also estimated
114 the seismic energy rate functions of tremors accompanied by VLFES to evaluate the scaled
115 energy of slow earthquakes around the Nicoya Peninsula.

116 **2. VLFES analysis**

117 **2.1. Data**

118 We used waveforms of a temporary seismic network, Tomography Under Costa Rica and
119 Nicaragua (TUCAN; Abers & Fischer, 2003), recorded from August 2004 to January 2006.
120 There were 49 broadband seismic stations in four lines (Figure 1b). In this study, we mainly used
121 data from stations in Costa Rica (shown in Figure 1a) for VLFES analysis. After removing
122 instrumental responses, the seismograms for VLFES detection were resampled at one sample per
123 second. We applied a bandpass filter in the frequency range of 0.02–0.05 Hz (e.g., Ghosh et al.,
124 2015; Ito et al., 2009; Takemura et al., 2019), because this frequency band is less affected by
125 microseismic noises (e.g., Kaneko et al., 2018).

126 **2.2. Matched-filter technique**

127 The detection procedure used for VLFES is similar to that used in our previous study
128 (Baba et al., 2020a). We used only the vertical component seismograms because the horizontal
129 component seismograms of many stations were noisy, and it was difficult to find VLFES signals
130 (Figure S1). We placed 175 virtual source grids on the Cocos Plate boundary at a uniform
131 interval of 0.1° (Figure 2a) and computed synthetic waveforms from these source grids to the
132 stations in Costa Rica using an open-source seismic wave propagation code (OpenSWPC; Maeda
133 et al., 2017). We used a three-dimensional velocity structure model constructed by combining
134 CRUST 1.0 (Laske et al., 2013), Slab2 (Hayes et al., 2018), and ETOPO1 (Amante & Eakins,
135 2009), setting the minimum S-wave velocity in the solid columns to 1.0 km/s. We adopted the
136 values of a mean oceanic slab structure (Christensen & Salisbury, 1975) for the physical
137 parameters of the subducting slab (Table S1). For the physical parameters of the other layers
138 except for the slab, we used the values of CRUST 1.0, and the default parameter set of
139 OpenSWPC. The model covered the region enclosed by the red line (Figure 1b), which was
140 discretized by a uniform grid interval of 0.2 km. The assumed VLFES moment rate function was a
141 Küpper wavelet with a source duration of 15 s and an M_w of 4.0 (Figure 4 of Maeda et al.,
142 2017). Since focal mechanisms of VLFES are consistent with shear slip on the plate boundaries
143 in previous studies (Cascadia: Ghosh et al., 2015; Nankai: Ito et al., 2009; Nakano et al., 2018;
144 Sugioka et al., 2012; Takemura et al., 2019), the focal mechanism at each source grid was
145 assumed to be consistent with the geometry of the plate boundary of Slab2 and the plate motion
146 model, NUVEL-1A (DeMets et al., 1994). The time window of each template was set to 150 s
147 from the event origin time. Hereafter, we simply refer to these synthetic waveforms as template
148 waveforms. Examples of template waveforms at updip and downdip source grids are shown in
149 Figures 2b and 2c, respectively. The signal first arrives at MANS and the variation of amplitudes

150 is small for the updip source, whereas signals first arriving at FINA exhibit amplitudes in or near
151 the Nicoya Peninsula that are much larger than in other areas for the downdip source.

152 We then calculated cross-correlation coefficients (CCs) between the filtered template
153 waveforms and observed seismograms every 1 s. We selected events with station-averaged
154 coefficients larger than a threshold defined as 9.5 times the median absolute deviation of the
155 distributions. In order to decrease false detections by non-VLFE signals, we adopted a strict
156 detection threshold compared to previous studies (e.g., Shelly et al., 2007). The changes of CCs
157 when focal mechanisms or depths of assumed source models are different from the geometry of
158 the plate boundary are shown in Figure S2.

159 **2.3. VLFE location and discarding false detections**

160 Although a strict detection threshold was employed, there are false detections that are
161 caused by other signals, such as local or regional regular earthquakes or teleseismic events. To
162 exclude local or regional earthquakes, we compared the origin time of detected events with a
163 catalog of local and regional regular earthquakes constructed by El Observatorio Vulcanológico
164 y Sismológico de Costa Rica, Universidad Nacional (Catálogo de Temblores de Costa Rica,
165 2004-2006; Protti, personal comm.). We discarded events whose epicentral distances were less
166 than 150 km and origin times were within ± 50 s from the local or regional earthquakes listed in
167 this earthquake catalog. To discard false detections by teleseismic events, we removed the events
168 detected between the P -wave arrivals and 600 s after S -wave arrivals of teleseismic events (M_w
169 ≥ 5) in the catalog of the United States Geological Survey. The event amplitudes and CCs are
170 positively correlated in general, but events with high amplitudes and low average CCs
171 occasionally appear. These events are considered to be false detections due to teleseismic events
172 absent in the catalogs. Therefore, we did not count events with average CCs below 0.56 and
173 relative amplitudes to templates higher than 0.4 (Baba et al., 2018; 2020a). If the amplitude
174 relative to the template with M_w of 4.0 was smaller than 0.05, we did not count the event
175 because the signal was too small to judge whether the event is truly existed or not.

176 For the remaining events, we calculated the variance reduction (VR) between the
177 template and observed waveforms. We estimated VRs using only the vertical component
178 seismograms of relatively quiet stations in and around the Nicoya Peninsula (MANS, CABA,
179 FINA, CRUP, and PALM), because differences of amplitude distributions between updip and
180 downdip events are large in these stations:

$$181 \quad VR = \left[1 - \frac{\sum_i \int \{f_i(t) - cg_i(t)\}^2 dt}{\sum_i \int \{f_i(t)\}^2 dt} \right] \times 100\% , \quad (1)$$

182 where $f_i(t)$ and $g_i(t)$ are the observed and template waveforms at the i -th station, respectively,
183 and c is the relative amplitude of the observed waveform to the template. We selected events
184 whose VRs were larger than 30%. This threshold is set by trial and error based on visual
185 identifications of VLFEs in the observed data.

186 After the above procedures, falsely detected events still remained because we only used
187 the vertical component seismograms, and the array configuration was cross shaped. To discard
188 the remaining false detections, we estimated the normalized-and-stacked amplitude, azimuth, and
189 velocity of signal propagation by applying delay-and-sum beamforming (Section 3.1 of Rost &
190 Thomas, 2002; Walter et al., 2013) to vertical component seismograms. After normalizing the
191 waveform of each station by its maximum amplitude in the 150 s time window, we searched for
192 the azimuth and velocity that maximized the stacked amplitude by performing a grid search for

193 the azimuth between 135° – 315° with 1° intervals and the velocity between 2–5 km/s with 0.1
194 km/s intervals. We first used the along-strike stations in both Costa Rica and Nicaragua (brown
195 inverted triangles in Figure 1b) to discard teleseismic events. The amplitudes of Costa Rican
196 VLFs at the Nicaraguan stations are generally very small compared with those in the Costa
197 Rican stations due to geometrical spreading, but amplitudes for teleseismic events are similar.
198 Therefore, we selected events whose stacked normalized amplitude normalized by the number of
199 stations was smaller than 0.6 because events with large stacked signals are suspected to be
200 teleseismic earthquakes (Figure S3). We then conducted another beamforming analysis for the
201 remaining events using the same stations as the matched-filter analysis, and selected events
202 whose azimuth was 200 – 230° . Finally, to avoid duplicate detection, only one event was counted
203 every 60 s from the remaining VLFE candidates. We only counted the event whose averaged CC
204 was the highest spatiotemporally.

205 **2.4. Estimation of the moments of events**

206 We estimated the source durations of detected VLFs by comparing template waveforms
207 with source durations of 10–50 s and an M_w of 4.0 with observed waveforms (e.g., Yabe et al.,
208 2021). The source duration that resulted in the highest values of CC between the observed and
209 template waveforms was adopted.

210 We also calculated the amplitude of an event relative to the template waveforms using the
211 same method as Baba et al. (2020b). The relative amplitude can be used to calculate the seismic
212 moment of each VLFE. The seismic moment rate of a VLFE was calculated by dividing its
213 seismic moment by its source duration.

214 **2.5. Characteristics of detected VLFs**

215 We detected 68 VLFs during the analysis period. Example traces of a VLFE located at
216 85.8°W and 9.4°N are shown in Figure 3. The signal of this VLFE first arrives at the MANS and
217 propagates to inland stations (top panel of Figure 3). This feature was successfully modeled for
218 the updip templates (Fig. 2b). There is a tremor signal in the frequency range of 2–8 Hz in the
219 same time window (middle and bottom panels of Figure 3). The cumulative number of VLFs
220 showed significant increases in September 2004 and August 2005 (Figure 4a). In August 2005,
221 an SSE was reported by Jiang et al. (2012); therefore, SSE and VLFE activities were temporally
222 correlated. The M_w and source duration of VLFs were mainly distributed in 3.4–4.2 and 10–30
223 s, respectively (Figures 5a, b). The M_w and source duration of VLFs have a positive correlation
224 (Figure 5c) like shallow VLFs in Nankai, Japan (Sugioka et al., 2012; Takemura et al., 2019).

225 Most of the VLFs (62 events) are distributed where the plate boundary is at a depth
226 range of 6–10 km below the sea level, near the trench axis off the Nicoya Peninsula (Figure 4b),
227 at the updip of the seismogenic zone. The distribution of these VLFs is consistent with the
228 VLFs in 2008 suggested by Walter et al. (2013). When locating some events using both vertical
229 and horizontal component seismograms whose signal to noise (SN) ratios are relatively high for
230 the verification of the analysis by using vertical components only, the high CC areas overlap and
231 the epicenters were also located near the trench axis, although there are differences of 0.1 – 0.2°
232 (Figure S1). The area overlaps with the shallower part of the large slip area of the 2007 SSE
233 (Jiang et al., 2017). Although the slip distribution of the 2005 SSE was not estimated in previous
234 studies, our results suggest that the 2005 SSE can also have a large slip area near the trench axis,
235 similar to the 2007 SSE. The distribution of VLFs lies within the gap between large slip areas

236 of thrust-type large interplate earthquakes with an M_w of 7–8 around the Nicoya Peninsula and
 237 the 1992 tsunami earthquake with an M_w of 7.6.

238 The distribution of the CC shows the resolution of the location of VLFs. By the
 239 distribution of CC, it is confirmed that most of the VLFs were located near the trench axis. CCs
 240 for more than half of the events exceeded the threshold only for updip templates (Figure 6a). For
 241 several events, CCs exceeded the threshold both updip and downdip of the seismogenic zone
 242 with a larger CC in the updip region (Figures 6b). On the other hand, 6 VLFs were located at a
 243 depth of ~ 40 km at the downdip of large earthquakes (Figure 4b). However, we cannot exclude
 244 the possibility that such VLFs occur in the updip region in real because, in such cases, two CC
 245 peaks tend to appear both in the updip and downdip (Figure 6c). Of course, there is a possibility
 246 that such VLFs really occur in the downdip region because the locations of such VLFs were
 247 near the locations of previously reported LFs (Brown et al. 2009) and tremors (Outerbridge et
 248 al. 2010). In this study, the SN ratios of VLFs detected in the downdip region are very low;
 249 hence, it is difficult to judge whether such VLFs occur in downdip or updip, because it is hard
 250 to judge which station the signal of the VLFE arrival first due to the similar arrival times at updip
 251 stations. The reason for the small number and the low SN ratio of downdip events may be that
 252 slow earthquakes in the downdip region were inactive during 1.5 years of the temporary array.
 253 To investigate whether deep VLFs really exist, an analysis with a longer dataset is needed in
 254 future work.

255 **3. Estimations of seismic energy rates for tremors accompanied by VLFs**

256 Tremor signals were also found in the frequency range of 2–8 Hz within the time
 257 windows of detected VLFs (middle panel of Figure 3). It is difficult to locate tremors in the
 258 offshore region by using an onshore network because sources of tremors are distant from the
 259 network and signals of tremors attenuate strongly compared to VLFE (0.02–0.05 Hz) signals.
 260 Based on the spatiotemporal correlation between VLFs and tremors reported in other regions
 261 (e.g., Ghosh et al., 2015; Maeda & Obara, 2009; Tamaribuchi et al., 2019) and the interpretation
 262 that VLFs and tremors are components of broadband slow earthquake phenomena (Gomberg et
 263 al., 2016; Hawthorne & Bartlow, 2018; Ide & Maury, 2018), we estimated the energy rate
 264 functions of tremors accompanied by VLFs by assuming that a tremor occurs at the same
 265 location as the VLFE.

266 We also used waveforms of the TUCAN network similarly to the VLFE detection. After
 267 applying a bandpass filter of 2–8 Hz, the envelope waveforms were calculated by taking the root-
 268 mean-square of sums of three-component squared seismograms and a smoothing time window of
 269 3 s (bottom panel of Figure 3). The envelope waveforms were resampled at one sample per
 270 second.

271 **3.1. Quality factor of the apparent S -wave attenuation**

272 To estimate the energy rate functions of tremors accurately, we estimated the quality
 273 factor of the apparent S -wave attenuation (Q_{app}), based on the coda-normalization method (e.g.,
 274 Aki, 1980; Yoshimoto et al., 1993). First, we selected some isolated regular earthquakes (Figure
 275 S4). To eliminate the effect of differences in source size and site amplification, observed
 276 maximum S -wave amplitudes were normalized by averaged coda amplitudes within a lapse time
 277 of 80–90 s. The coda-normalized maximum S -wave amplitude of the i -th earthquake at the j -th
 278 station (A_{ij}) and the distance between the hypocenter of the i -th earthquake and j -th station (L_{ij})
 279 have the following relationship (Takemura et al., 2017):

$$\ln(L_{ij}A_{ij}) = -\frac{\pi f_c Q_{app}^{-1}}{V_s} L_{ij} + C' , \quad (2)$$

where V_s is the S -wave velocity (assuming 3.5 km/s in this study; Maeda & Obara, 2009; Yabe et al., 2019; 2021), f_c is the central frequency (assuming 5 Hz in this study), and C' is a constant. By solving Equation (2) by the least-squares method, we estimated Q_{app}^{-1} as $10^{-2.42}$ (Figure 7a).

3.2. Site amplification factor

We estimated the site amplification factor at 2–8 Hz using relative coda amplitudes (e.g., Maeda and Obara, 2009). Coda amplitudes at a certain time window generally depend on the source size and site amplification (e.g., Chapters 2 and 3 of Sato et al., 2012). Therefore, the ratio of the coda wave amplitude at a station to that at a reference station for the same event depends only on the site amplification factor relative to a reference station.

We calculated the ratios of the coda amplitudes for each station to those of MANS (reference station) for each regular earthquake used in Section 3.1. The time window for evaluating relative coda amplitudes is the same as that in coda-normalization in Section 3.1. Then we calculated the average of the coda amplitude ratios of all earthquakes for each station. The estimated relative site amplification factors at each station used in the estimations of the energy rate functions of tremors are shown in Figure 7b. We compared coda amplitudes of regular earthquakes at MANS with those at the JTS, a permanent station of the Global Seismograph Network by Incorporated Research Institutions for Seismology and International Deployment of Accelerometers (Scripps Institution of Oceanography, 1986). The average ratio of coda amplitudes at MANS to those at JTS is 1.14, suggesting that the condition of MANS site is very similar to that of the JTS.

3.3. Seismic energy rate of tremors

By using apparent attenuation (Q_{app}^{-1}) and site amplification in the previous subsections, we estimated the energy rate functions of tremors. The source energy rate function of a tremor ($E_j(t)$) using the amplitude of the j -th station is calculated by the following formula (Maeda & Obara, 2009):

$$E_j(t) = 2\pi V_s r_j^2 \rho A_j'^2(t + t_j) \exp(2\pi f_c Q_{app}^{-1} t_j) , \quad (3)$$

where $A_j'(t)$ is the site-corrected amplitude of the envelope waveform of the j -th station, r_j is the hypocentral distance from the accompanying VLFE, t_j is the travel time from the VLFE source, and ρ is the density (assuming 2,700 kg/m³). For calculating $E_j(t)$, we used a 180 s time window that started 60 s before the origin time of VLFES. We calculated the CCs of all station pairs in Figure 7b. To estimate the source energy rate function of the tremor, we only used stations whose CCs with at least one other station exceeded 0.6.

The seismic energy rate W_j using the amplitude of the j -th station is given by the integration of the source energy rate function $E_j(t)$ in time:

$$W_j = \frac{1}{t_2 - t_1} \int_{t_1}^{t_2} E_j(t) dt , \quad (4)$$

where t_1 and t_2 are the start and end of the integration range, respectively. The integration range is defined as the period in which the values of $E_j(t)$ exceeded 20% of the maximum value of $E_j(t)$ (Figure 8). The seismic energy rate of a tremor (W_0) was obtained by calculating the

319 average W_j of all stations. The error of W_0 was obtained by calculating the standard deviation of
320 W_j .

321 The energy rates of tremors were mainly distributed in 10^3 – $10^{5.5}$ J/s (Figure 9). There is a
322 positive correlation between the energy rates of tremors and the moment rates of the
323 corresponding VLFs. We estimated the scaled energy by calculating the ratio between the
324 seismic energy rate of a tremor and the seismic moment rate of the corresponding VLFE. The
325 scaled energy of slow earthquakes off Costa Rica is mainly distributed in the range of 10^{-9} – 10^{-8}
326 (dotted lines in Figure 9).

327 **4. Discussion**

328 **4.1. shallow ETS off Costa Rica**

329 The activation of VLFs and tremors in August 2005 temporally correlates with the 2005
330 SSE reported by Jiang et al. (2012). VLFs and tremors occurred mainly in the updip area in
331 August 2005; hence, the slip area of the 2005 SSE can be distributed in the updip area near the
332 trench axis, similar to the 2007 SSE. In areas where shallow VLFs occurred, subseafloor
333 hydrological observatories recorded pore fluid pressure transients in 2000 (Brown et al., 2005),
334 2003–2004 (Solomon et al., 2009), and 2007–2013 (Davis et al., 2011; 2015). They interpreted
335 that pore fluid pressure transients were caused by SSEs. Spatial correspondence of pore fluid
336 change in the periods of previous studies and VLFE activity in 2005 near the trench off Costa
337 Rica suggests the occurrence of a shallow ETS, as with the Nankai subduction zone (Araki et al.,
338 2017; Nakano et al., 2018).

339 **4.2. Separation of slow earthquakes and other phenomena**

340 Before the 2012 Mw 7.6 earthquake, the interplate coupling of the shallow slow
341 earthquake area at a plate-boundary depth range of 6–10 km was expected to be very weak (Feng
342 et al., 2012)–unlike the coseismic slip area, which was strongly coupled (Protti et al., 2014). The
343 average stress drop of small-to-moderate regular earthquakes inside the large slip area of the
344 1992 tsunami earthquake (surrounded by dark blue lines in Figure 4) was 1.2 MPa, which was
345 smaller than that outside the large slip area (Bilek et al., 2016). The values of reported stress
346 drops of slow earthquakes in the Nankai subduction zone were 0.1–200 kPa (e.g., Ito & Obara,
347 2006; Takagi et al., 2019); therefore, we consider that the stress drops of slow earthquake area
348 are also much smaller than those of regular and tsunami earthquakes. The spatial variation of
349 interplate coupling and stress drop of slip at the plate boundary results from the heterogeneous
350 distribution of frictional properties at the plate boundary in the Central American subduction
351 zone. In addition, a low stress drop suggests a high pore pressure generated by the existence of
352 fluids (Yao & Yang, 2020). Therefore, the frictional strength of the slow earthquake area at a
353 depth range of 6–10 km can be quite weak owing to the rich fluid compared to that in the regions
354 with regular and tsunami earthquakes.

355 In Costa Rica, repeating earthquakes were activated after the 2012 Mw 7.6 earthquake
356 around the large coseismic slip area of the earthquake (Chaves et al., 2020). Such activation after
357 a large earthquake in the afterslip area was also observed in the Tohoku subduction zone (Uchida
358 & Matsuzawa, 2013). The locations of repeating earthquakes separate from the areas where
359 VLFs occur. Such separation is also found in the Nankai (e.g., Takemura et al., 2020) and the
360 Tohoku subduction zone (e.g., Nishikawa et al., 2019).

361 **4.3. Comparison with other subduction zones**

362 Our study revealed that shallow slow earthquakes occur near the trench axis off Costa
363 Rica, in the updip of coseismic slip areas of thrust-type large earthquakes with an M_w of 7–8.
364 The depth range and the separate distribution between shallow VLFs and large earthquakes off
365 Costa Rica are similar to shallow slow earthquakes in the Nankai subduction zone, where slow
366 earthquakes are spatially separated from high slip-deficit zones (e.g., Takemura et al., 2020). On
367 the other hand, before the 2011 Tohoku earthquake, shallow slow slip events propagated to the
368 initial rupture point of the great earthquake (Kato et al., 2012). Therefore, the characteristics of
369 distribution of slow and large earthquakes differ between Tohoku and Costa Rica.

370 There are other common features in shallow slow earthquakes between Costa Rica and
371 Nankai. Although the lower limit of M_w is large (~ 3.4) due to a strict threshold, the ranges of
372 magnitudes and source durations of shallow VLFs off Costa Rica are similar to those of
373 shallow VLFs in the Nankai subduction zones (e.g., Takemura et al., 2019). The recurrence
374 intervals of activation of slow earthquakes are one to several years in Costa Rica (Jiang et al.,
375 2012), which is similar to shallow slow earthquakes in the Nankai subduction zone, but different
376 from the shorter intervals of deep slow earthquakes in Nankai (e.g., Baba et al., 2020b).
377 Although the number of tremors whose energy rates are less than 10^4 J/s is small because of the
378 strict detection threshold of the corresponding VLFs, the upper limit of the energy rate range of
379 tremors is similar to that observed for shallow tremors in Nankai (Yabe et al., 2019). The
380 estimated scaled energy of slow earthquakes off Costa Rica is also similar to that of shallow slow
381 earthquakes in the Nankai subduction zone (Yabe et al., 2019). These results suggest that the
382 frictional properties within the shallow slow earthquake areas are similar in both Costa Rica and
383 Nankai. On the other hand, the scaled energy range in both regions is 0.5–1 orders of magnitude
384 larger than that of shallow slow earthquakes in the Tohoku subduction zone (Yabe et al., 2021),
385 and approximately 1 order of magnitude larger than that of deep slow earthquakes in Nankai (Ide
386 et al., 2008; Maeda & Obara, 2009).

387 The range of scaled energy and distribution of shallow slow earthquakes off Costa Rica
388 are more similar to those in shallow Nankai than shallow Tohoku. According to Syracuse et al.
389 (2010), the age and thermal parameters of Costa Rica are 15.8 Ma and 1,010 km, respectively,
390 which are closer to those of Nankai (20.0 Ma and 450 km, respectively) than Tohoku (115.2–
391 130.5 Ma and 5,720–6,040 km, respectively). In addition, the temperatures of shallower parts of
392 plate interfaces of these subduction zones are similar (Saffer & Wallace, 2015). On the other
393 hand, the Central American subduction zone is subduction of fast convergence rate (~ 8 cm/year;
394 DeMets et al., 1994), high dip angle, and erosional type (e.g., Bangs et al., 2016), which are
395 more similar to Tohoku than Nankai. Although the characteristics of slow earthquake activity
396 can be related to various factors, the thermal parameter and incoming plate age of Costa Rica is
397 more similar to Nankai than Tohoku. The temperature structure of the shallow plate interface is
398 probably most sensitive to incoming plate age (Maunder et al., 2019) and secondarily to thermal
399 parameter (Syracuse et al., 2010). Hence, similar temperature conditions on the interface may
400 explain the common features of shallow slow earthquakes off Costa Rica and in Nankai.

401 In previous studies, the large slip area of the SSE in 2007 was separated into deeper and
402 shallower parts (Jiang et al., 2017), and deep LFs and tremors were detected downdip of the
403 seismogenic zone (Brown et al., 2009; Outerbridge et al., 2010). If these deep LFs and tremors
404 occur in the downdip area, slow earthquakes might occur at separate depths along both shallower
405 and deeper extensions of rupture zones of large earthquakes (Figure 10). This characteristic
406 might also be the same as that of the Nankai subduction zone (Obara & Kato, 2016).

407 5. Conclusions

408 Based on the grid-search matched-filter technique using synthetic templates in the
 409 regional 3D model, we detected and located VLFs around the Nicoya Peninsula. Many VLFs
 410 occurred in September 2004 and August 2005, and most of the VLFs were located near the
 411 trench axis, where the plate boundary is at a depth range of 6–10 km, updip of the seismogenic
 412 zone. In this area, the occurrence of shallow SSEs is suggested by VLFE episodes. The region
 413 with VLFE activity overlaps with the shallower part of the large slip area of the 2007 SSE;
 414 therefore, the occurrences of shallow SSEs are suggested in September 2004 and August 2005 to
 415 occur in the same area as the shallower part of the 2007 SSE. The distribution of VLFs lies in
 416 the gap surrounding coseismic slip areas of tsunami and large regular earthquakes. This
 417 separation reflects the spatial distribution of the frictional strength of the plate boundary in the
 418 Central American subduction zone. By using high-frequency seismogram envelopes, we also
 419 estimated the energy rates of tremors accompanying VLFs. The ranges of magnitude and
 420 source duration of VLFs, energy rate of tremors, and scaled energy off Costa Rica are similar to
 421 those in shallow slow earthquakes in the Nankai subduction zone.

422 Data Availability

423 We used seismograms of the TUCAN network (Abers & Fischer, 2003;
 424 https://doi.org/10.7914/SN/YO_2003) and Global Seismograph Network (Scripps Institution of
 425 Oceanography, 1986; <https://doi.org/10.7914/SN/II>). We used the earthquake catalog of the U.S.
 426 Geological Survey (<https://earthquake.usgs.gov/earthquakes/search/>). We used OpenSWPC code
 427 Version 5.0.2 (Maeda et al., 2017; <https://doi.org/10.5281/zenodo.3712650>) for the numerical
 428 simulations. Numerical simulations were conducted using the Fujitsu PRIMERGY
 429 CX600M1/CX1640M1 (Oakforest-PACS) at the Information Technology Center, the University
 430 of Tokyo. We used generic mapping tools (Wessel et al., 2013) and Seismic Analysis Code
 431 (Helfrich et al., 2013) to prepare the figures and process seismograms, respectively. The VLFE
 432 and tremor catalog constructed by this study is provided in an open access repository, zenodo
 433 (doi: 10.5281/zenodo.4435232).

434 Acknowledgements

435 We would like to thank the editor, the associate editor and the two anonymous reviewers
 436 for their valuable comments and suggestions. We would like to thank Suguru Yabe for valuable
 437 discussions. We would also like to thank Marino Protti for providing the earthquake catalog in
 438 Costa Rica and for discussions. We thank Editage (www.editage.com) for English proofreading.
 439 This research was supported by JSPS KAKENHI Grant in Science Research on Innovative Areas
 440 “Science of Slow Earthquakes” (JP16H06473) and JSPS Research Fellowship DC1
 441 (JP19J20760). This study was also supported by the ERI-JURP 2020-S-04.

442 References

- 443 Abers, G. A., & Fischer, K. M. (2003). Tomography Under Costa Rica and Nicaragua.
 444 International Federation of Digital Seismograph Networks.
 445 https://doi.org/10.7914/SN/YO_2003
 446 Aki, K. (1980). Attenuation of shear-waves in the lithosphere for frequencies from 0.05 to 25 Hz.
 447 *Physics of the Earth and Planetary Interiors*, 21(1), 50–60. [https://doi.org/10.1016/0031-](https://doi.org/10.1016/0031-9201(80)90019-9)
 448 [9201\(80\)90019-9](https://doi.org/10.1016/0031-9201(80)90019-9)

- 449 Amante, C., & Eakins, B.W. (2009). ETOPO1 1 Arc-Minute Global Relief Model: Procedures,
450 Data Sources and Analysis. NOAA Technical Memorandum NESDIS NGDC-24.
451 <https://doi.org/10.7289/V5C8276M>
- 452 Araki, E., Saffer, D. M., Kopf, A. J., Wallace, L. M., Kimura, T., Machida, Y., et al. (2017).
453 Recurring and triggered slow-slip events near the trench at the Nankai Trough subduction
454 megathrust. *Science*, 356(6343), 1157–1160. <https://doi.org/10.1126/science.aan3120>
- 455 Baba, S., Takeo, A., Obara, K., Kato, A., Maeda, T., & Matsuzawa, T. (2018). Temporal
456 Activity Modulation of Deep Very Low Frequency Earthquakes in Shikoku, Southwest
457 Japan. *Geophysical Research Letters*, 45(2), 733–738.
458 <https://doi.org/10.1002/2017GL076122>
- 459 Baba, S., Takeo, A., Obara, K., Matsuzawa, T., & Maeda, T. (2020a). Comprehensive Detection
460 of Very Low Frequency Earthquakes Off the Hokkaido and Tohoku Pacific Coasts,
461 Northeastern Japan. *Journal of Geophysical Research: Solid Earth*, 125(1), 1–13.
462 <https://doi.org/10.1029/2019JB017988>
- 463 Baba, S., Takemura, S., Obara, K., & Noda, A. (2020b). Slow Earthquakes Illuminating
464 Interplate Coupling Heterogeneities in Subduction Zones. *Geophysical Research Letters*,
465 47(14), 4–5. <https://doi.org/10.1029/2020GL088089>
- 466 Bangs, N. L., McIntosh, K. D., Silver, E. A., Kluesner, J. W., & Ranero, C. R. (2016). A recent
467 phase of accretion along the southern Costa Rican subduction zone. *Earth and Planetary
468 Science Letters*, 443, 204–215. <https://doi.org/10.1016/j.epsl.2016.03.008>
- 469 Bilek, S. L., Rotman, H. M. M., & Phillips, W. S. (2016). Low stress drop earthquakes in the
470 rupture zone of the 1992 Nicaragua tsunami earthquake. *Geophysical Research Letters*,
471 43(19), 10,180–10,188. <https://doi.org/10.1002/2016GL070409>
- 472 Brown, J. R., Beroza, G. C., Ide, S., Ohta, K., Shelly, D. R., Schwartz, S. Y., et al. (2009). Deep
473 low-frequency earthquakes in tremor localize to the plate interface in multiple subduction
474 zones. *Geophysical Research Letters*, 36(19), 1–5. <https://doi.org/10.1029/2009GL040027>
- 475 Brown, K. M., Tryon, M. D., DeShon, H. R., Dorman, L. R. M., & Schwartz, S. Y. (2005).
476 Correlated transient fluid pulsing and seismic tremor in the Costa Rica subduction zone.
477 *Earth and Planetary Science Letters*, 238(1–2), 189–203.
478 <https://doi.org/10.1016/j.epsl.2005.06.055>
- 479 Chaves, E. J., Schwartz, S. Y., & Abercrombie, R. E. (2020). Repeating earthquakes record fault
480 weakening and healing in areas of megathrust postseismic slip, 2–10.
- 481 Christensen, N. I., & Salisbury, M. H. (1975). Structure and constitution of the lower oceanic
482 crust. *Reviews of Geophysics*, 13(1), 57–86. <https://doi.org/10.1029/RG013i001p00057>
- 483 Davis, E., Heesemann, M., & Wang, K. (2011). Evidence for episodic aseismic slip across the
484 subduction seismogenic zone off Costa Rica: CORK borehole pressure observations at the
485 subduction prism toe. *Earth and Planetary Science Letters*, 306(3–4), 299–305.
486 <https://doi.org/10.1016/j.epsl.2011.04.017>
- 487 Davis, E. E., Villinger, H., & Sun, T. (2015). Slow and delayed deformation and uplift of the
488 outermost subduction prism following ETS and seismogenic slip events beneath Nicoya
489 Peninsula, Costa Rica. *Earth and Planetary Science Letters*, 410, 117–127.
490 <https://doi.org/10.1016/j.epsl.2014.11.015>
- 491 DeMets, C., Gordon, R. G., Argus, D. F., & Stein, S. (1994). Effect of recent revisions to the
492 geomagnetic reversal time scale on estimates of current plate motions. *Geophysical
493 Research Letters*, 21(20), 2191–2194. <https://doi.org/10.1029/94GL02118>

- 494 Dixon, T. H., Jiang, Y., Malservisi, R., McCaffrey, R., Voss, N., Protti, M., & Gonzalez, V.
 495 (2014). Earthquake and tsunami forecasts: Relation of slow slip events to subsequent
 496 earthquake rupture. *Proceedings of the National Academy of Sciences of the United States*
 497 *of America*, *111*(48), 17039–17044. <https://doi.org/10.1073/pnas.1412299111>
- 498 Dragert, H., Wang, K., James, T. S. (2001). A Silent Slip Event on the Deeper Cascadia
 499 Subduction Interface. *Science*, *292*(5521), 1525–1528.
 500 <https://doi.org/10.1126/science.1060152>
- 501 Feng, L., Newman, A. V., Protti, M., Gonzalez, V., Jiang, Y., & Dixon, T. H. (2012). Active
 502 deformation near the Nicoya Peninsula, northwestern Costa Rica, between 1996 and 2010:
 503 Interseismic megathrust coupling. *Journal of Geophysical Research: Solid Earth*, *117*(6),
 504 1–23. <https://doi.org/10.1029/2012JB009230>
- 505 Ghosh, A., Huesca-Pérez, E., Brodsky, E., & Ito, Y. (2015). Very low frequency earthquakes in
 506 Cascadia migrate with tremor. *Geophysical Research Letters*, *42*(9), 3228–3232.
 507 <https://doi.org/10.1002/2015GL063286>
- 508 Gomberg, J., Wech, A., Creager, K., Obara, K., & Agnew, D. (2016). Reconsidering earthquake
 509 scaling. *Geophysical Research Letters*, *43*(12), 6243–6251.
 510 <https://doi.org/10.1002/2016GL069967>
- 511 Hawthorne, J. C., & Bartlow, N. M. (2018). Observing and Modeling the Spectrum of a Slow
 512 Slip Event. *Journal of Geophysical Research: Solid Earth*, *123*(5), 4243–4265.
 513 <https://doi.org/10.1029/2017JB015124>
- 514 Hayes, G. P., Moore, G. L., Portner, D. E., Hearne, M., Flamme, H., Furtney, M., & Smoczyk,
 515 G. M. (2018). Slab2, a Comprehensive Subduction Zone Geometry Model, *Science*,
 516 *61*(October), 58–61. <https://doi.org/10.1126/science.aat4723>
- 517 Helffrich, G., Wookey, J., & Bastow, I. (2013). *The Seismic Analysis Code*. Cambridge:
 518 Cambridge University Press. <https://doi.org/10.1017/CBO9781139547260>
- 519 Hutchison, A. A. (2020). Interepisodic Tremor and Slip Event Episodes of Quasi-
 520 spatiotemporally Discrete Tremor and Very Low Frequency Earthquakes in Cascadia
 521 Suggestive of a Connective Underlying, Heterogeneous Process. *Geophysical Research*
 522 *Letters*, *47*(3), 1–7. <https://doi.org/10.1029/2019GL086798>
- 523 Hutchison, A. A., & Ghosh, A. (2016). Very low frequency earthquakes spatiotemporally
 524 asynchronous with strong tremor during the 2014 episodic tremor and slip event in
 525 Cascadia. *Geophysical Research Letters*, *43*(13), 6876–6882.
 526 <https://doi.org/10.1002/2016GL069750>
- 527 Hutchison, A. A., & Ghosh, A. (2019). Repeating VLFs During ETS Events in Cascadia Track
 528 Slow Slip and Continue Throughout Inter-ETS Period. *Journal of Geophysical Research:*
 529 *Solid Earth*, *124*(1), 554–565. <https://doi.org/10.1029/2018JB016138>
- 530 Ide, S. (2016). Characteristics of slow earthquakes in the very low frequency band: Application
 531 to the Cascadia subduction zone. *Journal of Geophysical Research: Solid Earth*, *121*(8),
 532 5942–5952. <https://doi.org/10.1002/2016JB013085>
- 533 Ide, S., & Maury, J. (2018). Seismic Moment, Seismic Energy, and Source Duration of Slow
 534 Earthquakes: Application of Brownian slow earthquake model to three major subduction
 535 zones. *Geophysical Research Letters*, *45*(7), 3059–3067.
 536 <https://doi.org/10.1002/2018GL077461>
- 537 Ide, S., & Yabe, S. (2014). Universality of slow earthquakes in the very low frequency band.
 538 *Geophysical Research Letters*, *41*(8), 2786–2793. <https://doi.org/10.1002/2014GL059712>

- 539 Ide, S., Imanishi, K., Yoshida, Y., Beroza, G. C., & Shelly, D. R. (2008). Bridging the gap
540 between seismically and geodetically detected slow earthquakes. *Geophysical Research*
541 *Letters*, 35(10), 2–7. <https://doi.org/10.1029/2008GL034014>
- 542 Ito, Y., Obara, K., Shiomi, K., Sekine, S., & Hirose, H. (2007). Slow Earthquakes Coincident
543 with Episodic Tremors and Slow Slip Events. *Science*, 315(5811), 503–506.
544 <https://doi.org/10.1126/science.1134454>
- 545 Ito, Y., & Obara, K. (2006). Very low frequency earthquakes within accretionary prisms are very
546 low stress-drop earthquakes. *Geophysical Research Letters*, 33(9), 1–4.
547 <https://doi.org/10.1029/2006GL025883>
- 548 Ito, Y., Obara, K., Matsuzawa, T., & Maeda, T. (2009). Very low frequency earthquakes related
549 to small asperities on the plate boundary interface at the locked to aseismic transition.
550 *Journal of Geophysical Research: Solid Earth*, 114(11), 1–16.
551 <https://doi.org/10.1029/2008JB006036>
- 552 Ito, Y., Hino, R., Kido, M., Fujimoto, H., Osada, Y., Inazu, D., Ohta, Y., Iinuma, T., Ohzono,
553 M., Miura, S., Mishina, M., Suzuki, K., Tsuji, T., & Ashi, J. (2013). Episodic slow slip
554 events in the Japan subduction zone before the 2011 Tohoku-Oki earthquake.
555 *Tectonophysics*, 600, 14–26. <https://doi.org/10.1016/j.tecto.2012.08.022>
- 556 Jiang, Y., Wdowinski, S., Dixon, T. H., Hackl, M., Protti, M., & Gonzalez, V. (2012). Slow slip
557 events in Costa Rica detected by continuous GPS observations, 2002–2011. *Geochemistry,*
558 *Geophysics, Geosystems*, 13(1), 1–18. <https://doi.org/10.1029/2012GC004058>
- 559 Jiang, Y., Liu, Z., Davis, E. E., Schwartz, S. Y., Dixon, T. H., Voss, N., et al. (2017). Strain
560 release at the trench during shallow slow slip: The example of Nicoya Peninsula, Costa
561 Rica. *Geophysical Research Letters*, 44(10), 4846–4854.
562 <https://doi.org/10.1002/2017GL072803>
- 563 Kanamori, H., & Rivera, L. (2006). Energy partitioning during an earthquake. *Geophysical*
564 *Monograph Series*, 170, 3–13. <https://doi.org/10.1029/170GM03>
- 565 Kaneko, L., Ide, S., & Nakano, M. (2018). Slow Earthquakes in the Microseism Frequency Band
566 (0.1–1.0 Hz) off Kii Peninsula, Japan. *Geophysical Research Letters*, 45(6), 2618–2624.
567 <https://doi.org/10.1002/2017GL076773>
- 568 Kato, A., & Nakagawa, S. (2014). Multiple slow-slip events during a foreshock sequence of the
569 2014 Iquique, Chile Mw 8.1 earthquake. *Geophysical Research Letters*, 41, 6413–6419.
570 <https://doi.org/10.1002/2014GL061184>
- 571 Kato, A., Obara, K., Igarashi, T., Tsuruoka, H., Nakagawa, S., & Hirata, N. (2012). Propagation
572 of Slow Slip Leading Up to the 2011 Mw 9.0 Tohoku-Oki Earthquake. *Science*, 335(6069),
573 705–708. <https://doi.org/10.1126/science.1215141>
- 574 Laske, G., Masters, G., Ma, Z., & Pasyanos, M. (2013). Update on CRUST1.0 - A 1-degree
575 Global Model of Earth's Crust, Paper presented at EGU General Assembly, European
576 Geoscience Union, Vienna
- 577 Maeda, T., & Obara, K. (2009). Spatiotemporal distribution of seismic energy radiation from
578 low-frequency tremor in western Shikoku, Japan. *Journal of Geophysical Research: Solid*
579 *Earth*, 114(10). <https://doi.org/10.1029/2008JB006043>
- 580 Maeda, T., Takemura, S., & Furumura, T. (2017). OpenSWPC: An open-source integrated
581 parallel simulation code for modeling seismic wave propagation in 3D heterogeneous
582 viscoelastic media 4. *Seismology. Earth, Planets and Space*, 69(1).
583 <https://doi.org/10.1186/s40623-017-0687-2>

- 584 Maunder, B., van Hunen, J., Bouilhol, P., & Magni, V. (2019). Modeling Slab Temperature: A
 585 Reevaluation of the Thermal Parameter. *Geochemistry, Geophysics, Geosystems*, 20(2),
 586 673–687. <https://doi.org/10.1029/2018GC007641>
- 587 Nadeau, R. M., & Dolenc, D. (2005). Nonvolcanic tremors deep beneath the San Andreas Fault.
 588 *Science*, 307(5708), 389. <https://doi.org/10.1126/science.1107142>
- 589 Nakano, M., Hori, T., Araki, E., Kodaira, S., & Ide, S. (2018). Shallow very-low-frequency
 590 earthquakes accompany slow slip events in the Nankai subduction zone /704/2151/210
 591 /704/2151/508 article. *Nature Communications*, 9(1). [https://doi.org/10.1038/s41467-018-](https://doi.org/10.1038/s41467-018-03431-5)
 592 03431-5
- 593 Nishikawa, T., Matsuzawa, T., Ohta, K., Uchida, N., Nishimura, T., & Ide, S. (2019). The slow
 594 earthquake spectrum in the Japan Trench illuminated by the S-net seafloor observatories.
 595 *Science (New York, N.Y.)*, 365(6455), 808–813. <https://doi.org/10.1126/science.aax5618>
- 596 Obara, K. (2002). Nonvolcanic Deep Tremor Associated with Subduction in Southwest Japan.
 597 *Science*, 296(5573), 1679–1681. <https://doi.org/10.1126/science.1070378>
- 598 Obara, K. (2011). Characteristics and interactions between non-volcanic tremor and related slow
 599 earthquakes in the Nankai subduction zone, southwest Japan. *Journal of Geodynamics*,
 600 52(3–4), 229–248. <https://doi.org/10.1016/j.jog.2011.04.002>
- 601 Obara, K., & Ito, Y. (2005). Very low frequency earthquakes excited by the 2004 off Kii
 602 peninsula earthquakes: A dynamic deformation process in the large accretionary prism.
 603 *Earth, Planets and Space*, 57(4), 321–326. <https://doi.org/10.1186/BF03352570>
- 604 Obara, K., & Kato, A. (2016). Connecting slow earthquakes to huge earthquakes. *Science (New*
 605 *York, N.Y.)*, 353(6296), 253–257. <https://doi.org/10.1126/science.aaf1512>
- 606 Outerbridge, K. C., Dixon, T. H., Schwartz, S. Y., Walter, J. I., Protti, M., Gonzalez, V., et al.
 607 (2010). A tremor and slip event on the Cocos-Caribbean subduction zone as measured by a
 608 global positioning system (GPS) and seismic network on the Nicoya Peninsula, Costa Rica.
 609 *Journal of Geophysical Research: Solid Earth*, 115(10), 1–17.
 610 <https://doi.org/10.1029/2009JB006845>
- 611 Protti, M. (1995). The March 25, 1990 (Mw=7.0, ML=6.8), earthquake at the entrance of the
 612 Nicoya Gulf, Costa Rica: its prior activity, foreshocks, aftershocks, and triggered seismicity.
 613 *Journal of Geophysical Research*, 100(B10), 345–358. <https://doi.org/10.1029/94jb03099>
- 614 Protti, M., González, V., Newman, A. V., Dixon, T. H., Schwartz, S. Y., Marshall, J. S., et al.
 615 (2014). Nicoya earthquake rupture anticipated by geodetic measurement of the locked plate
 616 interface. *Nature Geoscience*, 7(2), 117–121. <https://doi.org/10.1038/ngeo2038>
- 617 Rogers, G., & Dragert, H. (2003). Episodic Tremor and Slip on the Cascadia Subduction Zone:
 618 The Chatter of Silent Slip. *Science*, 300(5627), 1942–1943.
 619 <https://doi.org/10.1126/science.1084783>
- 620 Rost, S., & Thomas, C. (2002). Array seismology: Methods and applications. *Reviews of*
 621 *Geophysics*, 40(3), 2-1-2–27. <https://doi.org/10.1029/2000RG000100>
- 622 Ruiz, S., Aden-Antoniow, F., Baez, J. C., Otarola, C., Potin, B., del Campo, F., et al. (2017).
 623 Nucleation Phase and Dynamic Inversion of the M w 6.9 Valparaíso 2017 Earthquake in
 624 Central Chile. *Geophysical Research Letters*, 44(20), 10,290-10,297.
 625 <https://doi.org/10.1002/2017GL075675>
- 626 Saffer, D. M., & Wallace, L. M. (2015). The frictional, hydrologic, metamorphic and thermal
 627 habitat of shallow slow earthquakes. *Nature Geoscience*, 8(8), 594–600.
 628 <https://doi.org/10.1038/ngeo2490>

- 629 Satake, K. (1994). Mechanism of the 1992 Nicaragua Tsunami Earthquake. *Geophysical*
630 *Research Letters*, 21(23), 2519–2522. <https://doi.org/10.1029/94GL02338>
- 631 Sato, H., Fehler, M., & Maeda, T. (2012). *Seismic Wave Propagation and Scattering in the*
632 *Heterogeneous Earth Structure*, 2nd ed., New York, Springer-Verlag.
- 633 Scripps Institution of Oceanography. (1986). IRIS/IDA Seismic Network. International
634 Federation of Digital Seismograph Networks. <https://doi.org/10.7914/SN/II>
- 635 Shelly, D. R., Beroza, G. C., Ide, S., & Nakamura, S. (2006). Low-frequency earthquakes in
636 Shikoku, Japan, and their relationship to episodic tremor and slip. *Nature*, 442(7099), 188–
637 191. <https://doi.org/10.1038/nature04931>
- 638 Shelly, D. R., Beroza, G. C., & Ide, S. (2007). Non-volcanic tremor and low-frequency
639 earthquake swarms. *Nature*, 446(7133), 305–307. <https://doi.org/10.1038/nature05666>
- 640 Solomon, E. A., Kastner, M., Wheat, C. G., Jannasch, H., Robertson, G., Davis, E. E., & Morris,
641 J. D. (2009). Long-term hydrogeochemical records in the oceanic basement and forearc
642 prism at the Costa Rica subduction zone. *Earth and Planetary Science Letters*, 282(1–4),
643 240–251. <https://doi.org/10.1016/j.epsl.2009.03.022>
- 644 Sugioka, H., Okamoto, T., Nakamura, T., Ishihara, Y., Ito, A., Obana, K., et al. (2012).
645 Tsunamigenic potential of the shallow subduction plate boundary inferred from slow
646 seismic slip. *Nature Geoscience*, 5(6), 414–418. <https://doi.org/10.1038/ngeo1466>
- 647 Syracuse, E. M., van Keken, P. E., Abers, G. A., Suetsugu, D., Bina, C., Inoue, T., et al. (2010).
648 The global range of subduction zone thermal models. *Physics of the Earth and Planetary*
649 *Interiors*, 183(1–2), 73–90. <https://doi.org/10.1016/j.pepi.2010.02.004>
- 650 Takagi, R., Uchida, N., & Obara, K. (2019). Along-Strike Variation and Migration of Long-
651 Term Slow Slip Events in the Western Nankai Subduction Zone, Japan. *Journal of*
652 *Geophysical Research: Solid Earth*, (Figure 1), 3853–3880.
653 <https://doi.org/10.1029/2018JB016738>
- 654 Takemura, S., Kobayashi, M., & Yoshimoto, K. (2017). High-frequency seismic wave
655 propagation within the heterogeneous crust: Effects of seismic scattering and intrinsic
656 attenuation on ground motion modelling. *Geophysical Journal International*, 210(3), 1806–
657 1822. <https://doi.org/10.1093/gji/ggx269>
- 658 Takemura, S., Matsuzawa, T., Noda, A., Tonegawa, T., Asano, Y., Kimura, T., & Shiomi, K.
659 (2019). Structural Characteristics of the Nankai Trough Shallow Plate Boundary Inferred
660 From Shallow Very Low Frequency Earthquakes. *Geophysical Research Letters*, 46(8),
661 4192–4201. <https://doi.org/10.1029/2019GL082448>
- 662 Takemura, S., Okuwaki, R., Kubota, T., Shiomi, K., Kimura, T., & Noda, A. (2020). Centroid
663 moment tensor inversions of offshore earthquakes using a three-dimensional velocity
664 structure model: slip distributions on the plate boundary along the Nankai Trough.
665 *Geophysical Journal International*, 222(2), 1109–1125. <https://doi.org/10.1093/gji/ggaa238>
- 666 Tamaribuchi, K., Kobayashi, A., Nishimiya, T., Hirose, F., & Annoura, S. (2019).
667 Characteristics of Shallow Low-Frequency Earthquakes off the Kii Peninsula, Japan, in
668 2004 Revealed by Ocean Bottom Seismometers. *Geophysical Research Letters*, 46(23),
669 13737–13745. <https://doi.org/10.1029/2019GL085158>
- 670 Uchida, N., & Matsuzawa, T. (2013). Pre- and postseismic slow slip surrounding the 2011
671 Tohoku-oki earthquake rupture. *Earth and Planetary Science Letters*, 374, 81–91.
672 <https://doi.org/10.1016/j.epsl.2013.05.021>

- 673 Voss, N., Dixon, T. H., Liu, Z., Malservisi, R., Protti, M., & Schwartz, S. (2018). Do slow slip
674 events trigger large and great megathrust earthquakes? *Science Advances*, 4(10), 1–6.
675 <https://doi.org/10.1126/sciadv.aat8472>
- 676 Voss, N. K., Malservisi, R., Dixon, T. H., & Protti, M. (2017). Slow slip events in the early part
677 of the earthquake cycle. *Journal of Geophysical Research: Solid Earth*, 122(8), 6773–6786.
678 <https://doi.org/10.1002/2016JB013741>
- 679 Walter, J. I., Schwartz, S. Y., Protti, J. M., & Gonzalez, V. (2011). Persistent tremor within the
680 northern Costa Rica seismogenic zone. *Geophysical Research Letters*, 38(1), 1–5.
681 <https://doi.org/10.1029/2010GL045586>
- 682 Walter, J. I., Schwartz, S. Y., Protti, M., & Gonzalez, V. (2013). The synchronous occurrence of
683 shallow tremor and very low frequency earthquakes offshore of the Nicoya Peninsula, Costa
684 Rica. *Geophysical Research Letters*, 40(8), 1517–1522. <https://doi.org/10.1002/grl.50213>
- 685 Wang, L., & Barbot, S. (2020). Excitation of San Andreas tremors by thermal instabilities below
686 the seismogenic zone. *Science Advances*, 6(36). <https://doi.org/10.1126/sciadv.abb2057>
- 687 Wessel, P., Smith, W. H. F., Scharroo, R., Luis, J., & Wobbe, F. (2013). Generic mapping tools:
688 Improved version released. *Eos*, 94(45), 409–410. <https://doi.org/10.1002/2013EO450001>
- 689 Xie, S., Dixon, T. H., Malservisi, R., Jiang, Y., Protti, M., & Muller, C. (2020). Slow Slip and
690 Inter-transient Locking on the Nicoya Megathrust in the Late and Early Stages of an
691 Earthquake Cycle. *Journal of Geophysical Research: Solid Earth*, 125(11), 1–22.
692 <https://doi.org/10.1029/2020JB020503>
- 693 Yabe, S., Tonegawa, T., & Nakano, M. (2019). Scaled Energy Estimation for Shallow Slow
694 Earthquakes. *Journal of Geophysical Research: Solid Earth*, 124(2), 1507–1519.
695 <https://doi.org/10.1029/2018JB016815>
- 696 Yabe, S., Baba, S., Tonegawa, T., Nakano, M., & Takemura, S. (2021). Seismic energy radiation
697 and along-strike heterogeneities of shallow tectonic tremors at the Nankai Trough and Japan
698 Trench. *Tectonophysics*, 228714. <https://doi.org/10.1016/j.tecto.2020.228714>
- 699 Yao, S., & Yang, H. (2020). Rupture Dynamics of the 2012 Nicoya Mw 7.6 Earthquake:
700 Evidence for Low Strength on the Megathrust. *Geophysical Research Letters*, 47(13), 1–11.
701 <https://doi.org/10.1029/2020GL087508>
- 702 Yokota, Y., & Ishikawa, T. (2020). Shallow slow slip events along the Nankai Trough detected
703 by GNSS-A. *Science Advances*, 6(3), 1–12. <https://doi.org/10.1126/sciadv.aay5786>
- 704 Yoshimoto, K., Sato, H., & Ohtake, M. (1993). Frequency-Dependent Attenuation of P and S
705 Waves In the Kanto Area, Japan, Based On the Coda-Normalization Method. *Geophysical*
706 *Journal International*, 114(1), 165–174. [https://doi.org/10.1111/j.1365-](https://doi.org/10.1111/j.1365-246X.1993.tb01476.x)
707 [246X.1993.tb01476.x](https://doi.org/10.1111/j.1365-246X.1993.tb01476.x)
- 708 Yue, H., Lay, T., Schwartz, S. Y., Rivera, L., Protti, M., Dixon, T. H., et al. (2013). The 5
709 September 2012 Nicoya, Costa Rica Mw 7.6 earthquake rupture process from joint
710 inversion of high-rate GPS, strong-motion, and teleseismic P wave data and its relationship
711 to adjacent plate boundary interface properties. *Journal of Geophysical Research: Solid*
712 *Earth*, 118(10), 5453–5466. <https://doi.org/10.1002/jgrb.50379>

713 **Figure captions**

714 **Figure 1.** (a) Large regular and slow earthquake areas based on previous studies around the
715 Nicoya Peninsula, in Costa Rica. Green contours show the coseismic slip distribution of the 2012
716 Mw 7.6 earthquake with a 1-m interval (Yue et al., 2013). Blue and dark blue areas show the slip
717 areas of large and tsunami earthquakes (1990 Mw 7.3: Protti et al., 1995; others: Yue et al.,

718 2013). Orange ellipses with dashed lines show large slip areas of the 2007 SSE (Jiang et al.,
 719 2017). The orange ellipse with a solid line shows the distributions of LFEs (Brown et al., 2009)
 720 and tremors (Outerbridge et al., 2010). Black inverted triangles show the station locations of the
 721 TUCAN network used in VLFE detection (Section 2.2). (b) Map of the Central American
 722 subduction zone. Solid line represents the Middle America Trench (Slab2; Hayes et al., 2018).
 723 Dashed contours indicate the isodepths of the top of the Cocos Plate with 10 km intervals (Slab2;
 724 Hayes et al., 2018). Black arrow indicates the convergence direction of the Cocos Plate, which
 725 subducts below the Caribbean plate from the Middle America Trench (NUVEL-1A; DeMets et
 726 al., 1994). Inverted triangles show the locations of stations of the TUCAN network. Brown
 727 triangles are stations which were used in beamforming (Section 2.3). The black lines in the inset
 728 show plate boundaries.

729 **Figure 2.** (a) Virtual source grids assumed in this study. Beach balls show the locations and focal
 730 mechanisms of the virtual sources. Inverted triangles and the black line are the same as in Figure
 731 1. Dashed contours indicate the isodepths of the top of the Cocos Plate with 10 km intervals
 732 (Slab2; Hayes et al., 2018). Examples of waveforms of virtual sources in the (b) updip and (c)
 733 downdip areas. Sources of Figures 1b and 1c are shown by the red and blue beachballs in Figure
 734 2a, respectively.

735 **Figure 3.** Example of waveforms of a VLFE and the corresponding tremor located at 85.8°W
 736 and 9.4°N (shown by a red beachball in Figure 2a) in the frequency range of 0.02–0.05 Hz and
 737 2–8 Hz, and smoothed root-mean-square envelope in the frequency range of 2–8 Hz.
 738 Seismograms are shown from the origin time of the VLFE, 03:53:47 (UTC), August 10, 2005.

739 **Figure 4.** (a) Cumulative number of the VLFEs from July 2004 to January 2006. Gray shading
 740 shows the period of the 2005 SSE (Jiang et al., 2012). (b) Distribution of the number of detected
 741 events at each virtual source. Blue ellipses and polygons, dark blue quadrangle, inverted
 742 triangles, black line, and dashed contours are the same as in Figure 1.

743 **Figure 5.** Distribution of (a) magnitudes and (b) source durations of VLFEs. (c) Relationship
 744 between source durations and magnitudes of VLFEs.

745 **Figure 6.** Examples of CC distributions of (a) an event which has large CCs only in updip grids,
 746 (b) an event which has large CCs both in updip and downdip grids but is located in an updip grid,
 747 and (c) an event which has large CCs both in updip and downdip grids but is located in a
 748 downdip grid. Inverted triangles, black line, and dashed contours are the same as in Figure 1.

749 **Figure 7.** (a) Relationship between logarithm of coda-normalized maximum *S*-wave amplitudes
 750 and hypocentral distances. To eliminate effects of geometrical spreading of *S*-wave, coda-
 751 nomadized *S*-wave amplitudes were multiplied by their hypocentral distance. Red line shows the
 752 regression line using Equation (2). (b) Site amplification factors relative to MANS based on
 753 relative coda amplitude measurements.

754 **Figure 8.** Temporal changes of energy rate functions of a tremor in (a) MANS and CABA and
 755 (b) PUCA and FINA. The corresponding VLFE occurs on 03:53:47 (UTC), August 10, 2012.
 756 Dashed lines indicate the threshold, which is set as 20% of the maximum value of the energy rate
 757 functions.

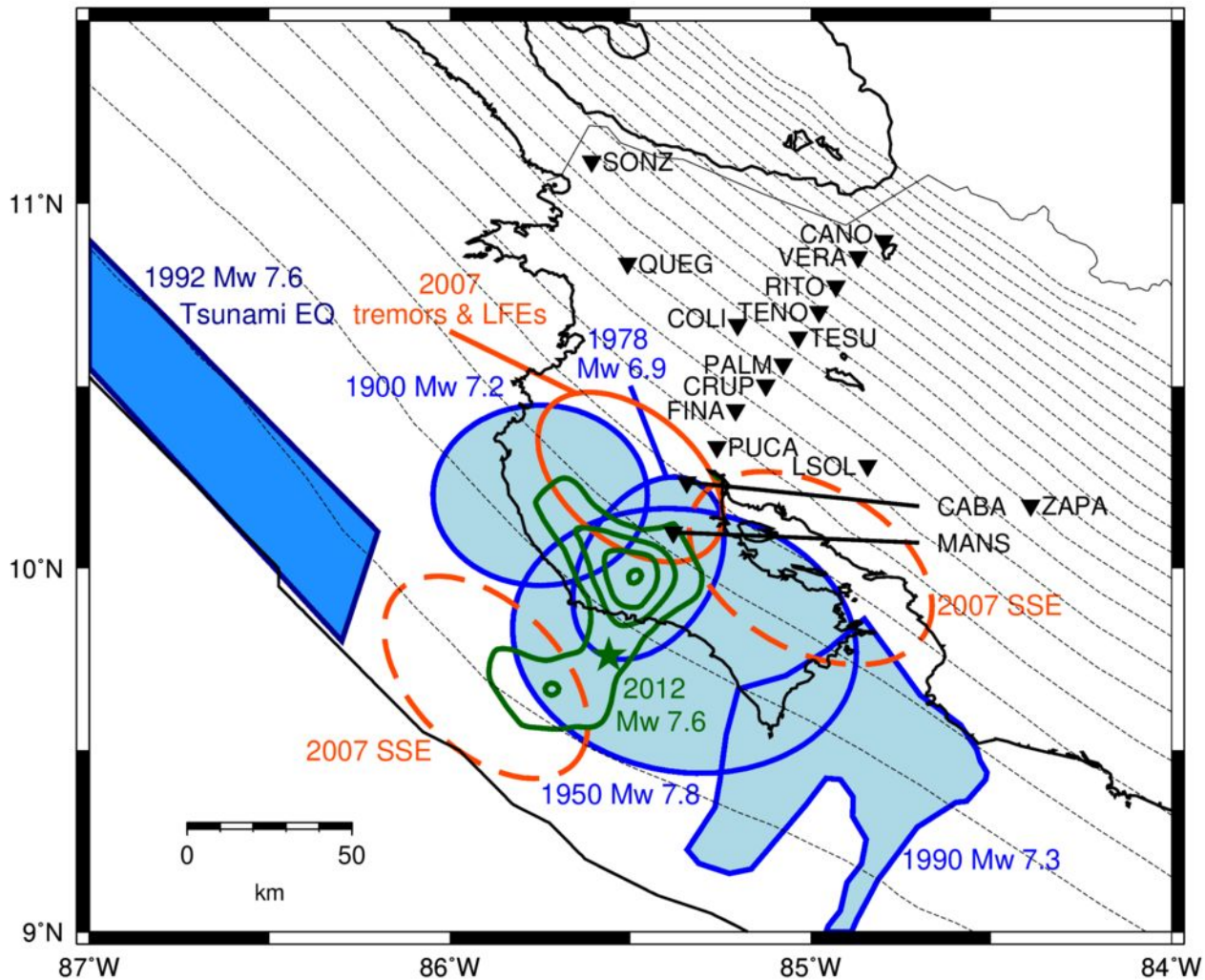
758 **Figure 9.** Relationship between seismic moment rates of VLFEs and seismic moment rates of
759 tremors estimated in this study. Red circles and blue diamonds show the events of updip and
760 downdip regions, respectively. Dashed lines show scaled energies of 10^{-7} , 10^{-8} , 10^{-9} , and 10^{-10} .
761 Orange shadings show the distributions of shallow slow earthquakes in the Nankai (Yabe et al.,
762 2019) and Tohoku subduction zones (Yabe et al., 2021), and deep slow earthquakes in southwest
763 Japan (Ide & Yabe, 2014), Cascadia (Ide, 2016), and Mexico (Ide & Maury, 2018).

764 **Figure 10.** A schematic illustration showing the interpretation of distributions of slow, tsunami,
765 and large regular earthquakes in the Central American subduction zone. The areas of large
766 earthquakes, the 1992 tsunami earthquake, and deep slow earthquakes are referred from Yue et
767 al. (2013), Satake (1994), and Outerbridge et al. (2010), respectively.

768
769
770

Figure 1.

(a) Costa Rica



(b) Central American subduction zone

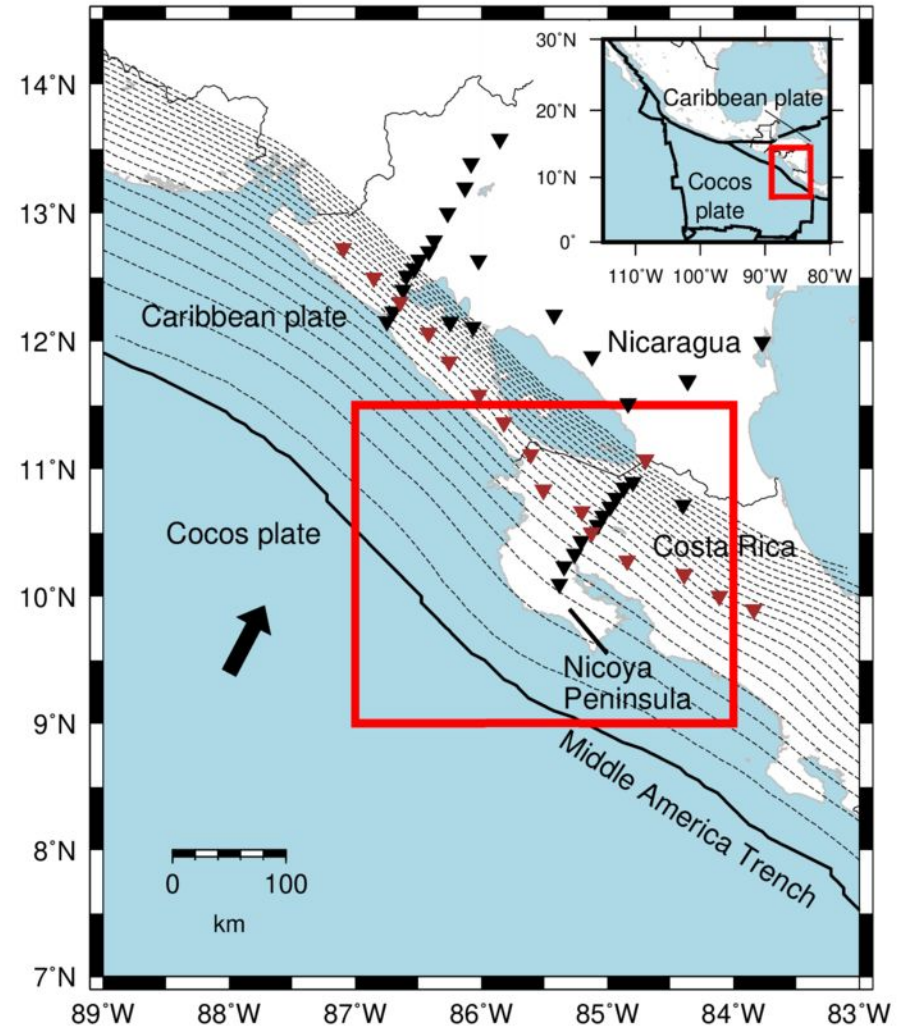
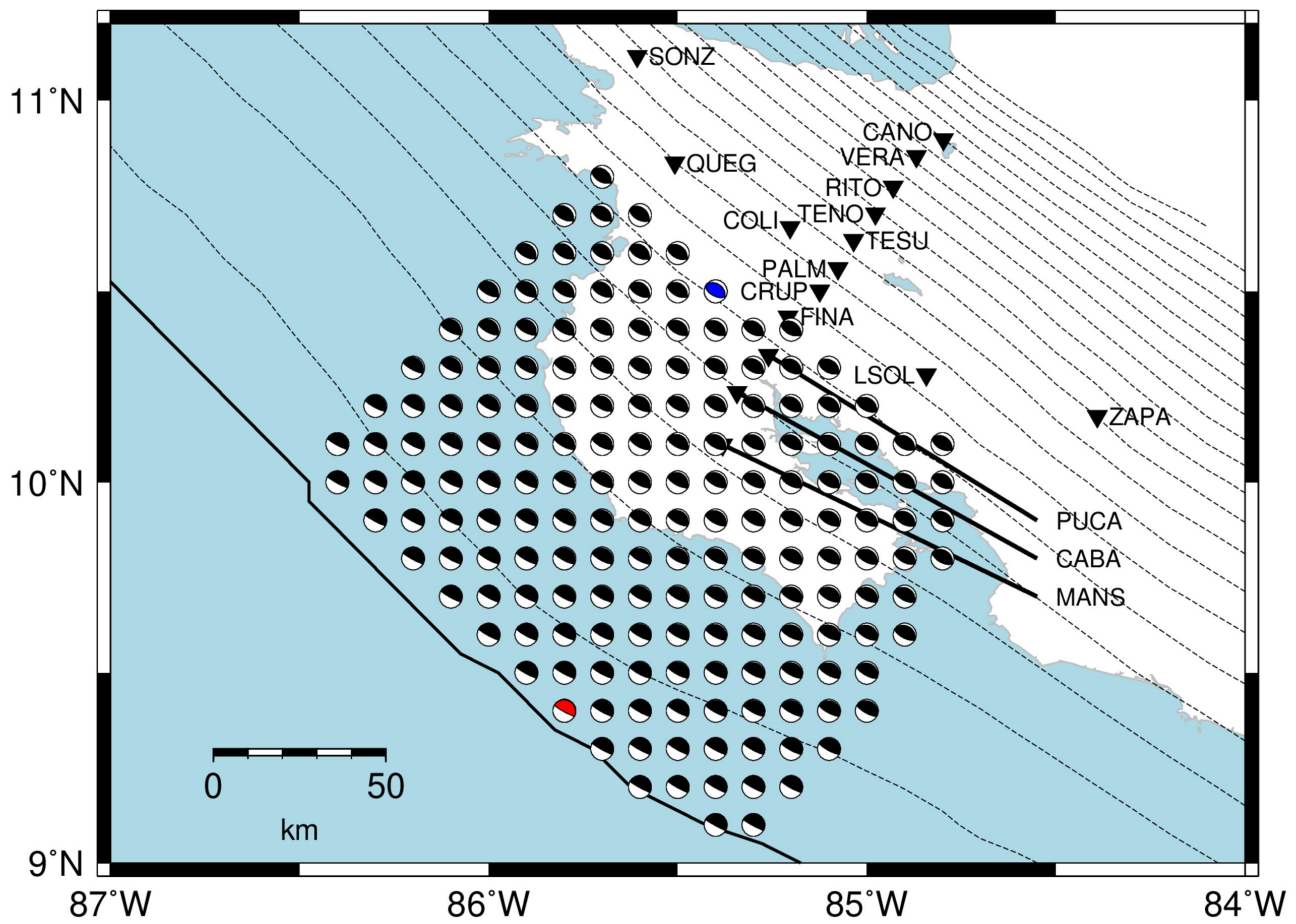
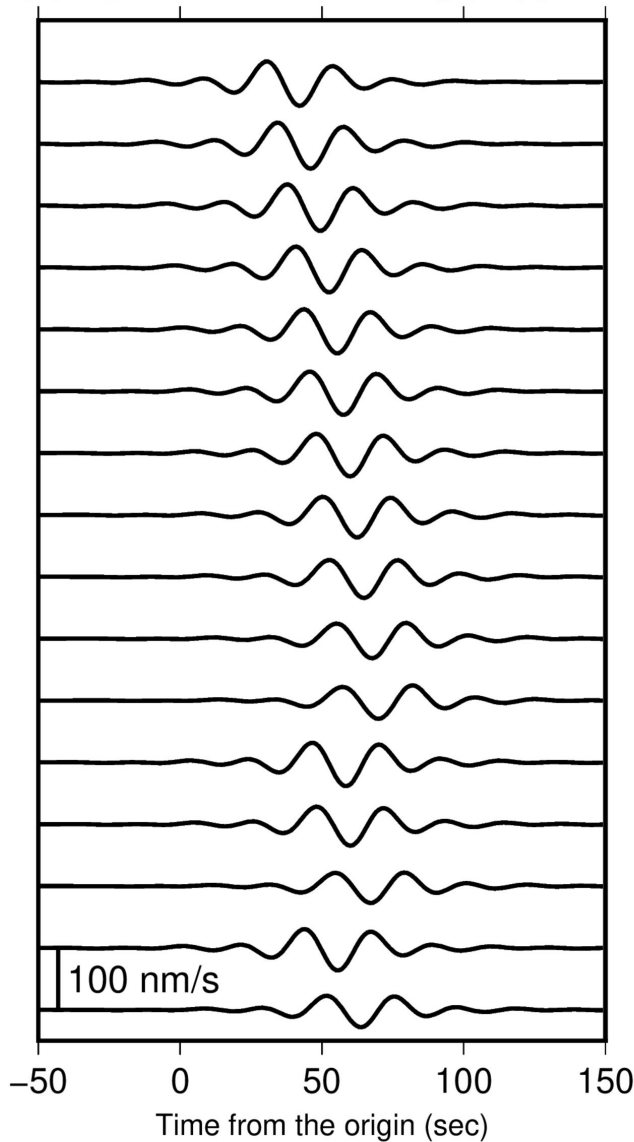


Figure 2.

(a)



(b) Synthetic waveforms (updip)



(c) Synthetic waveforms (downdip)

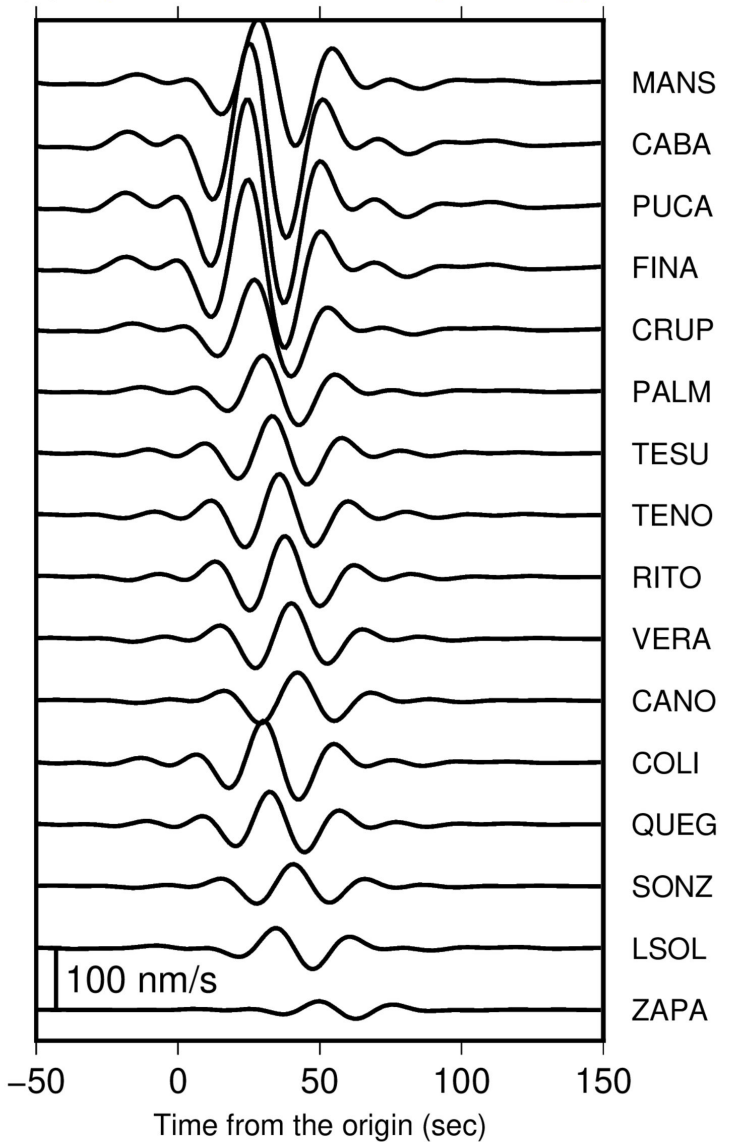


Figure 3.

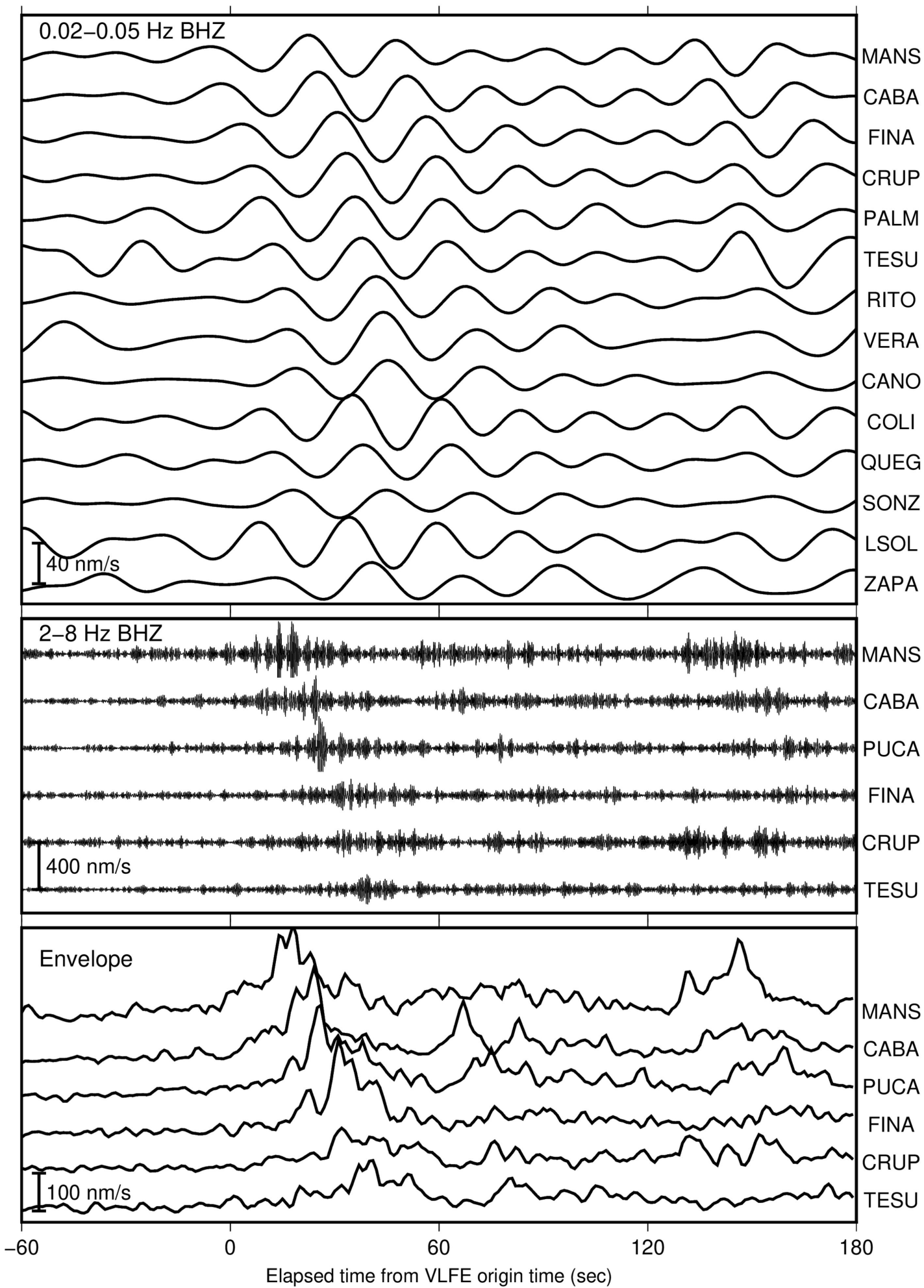
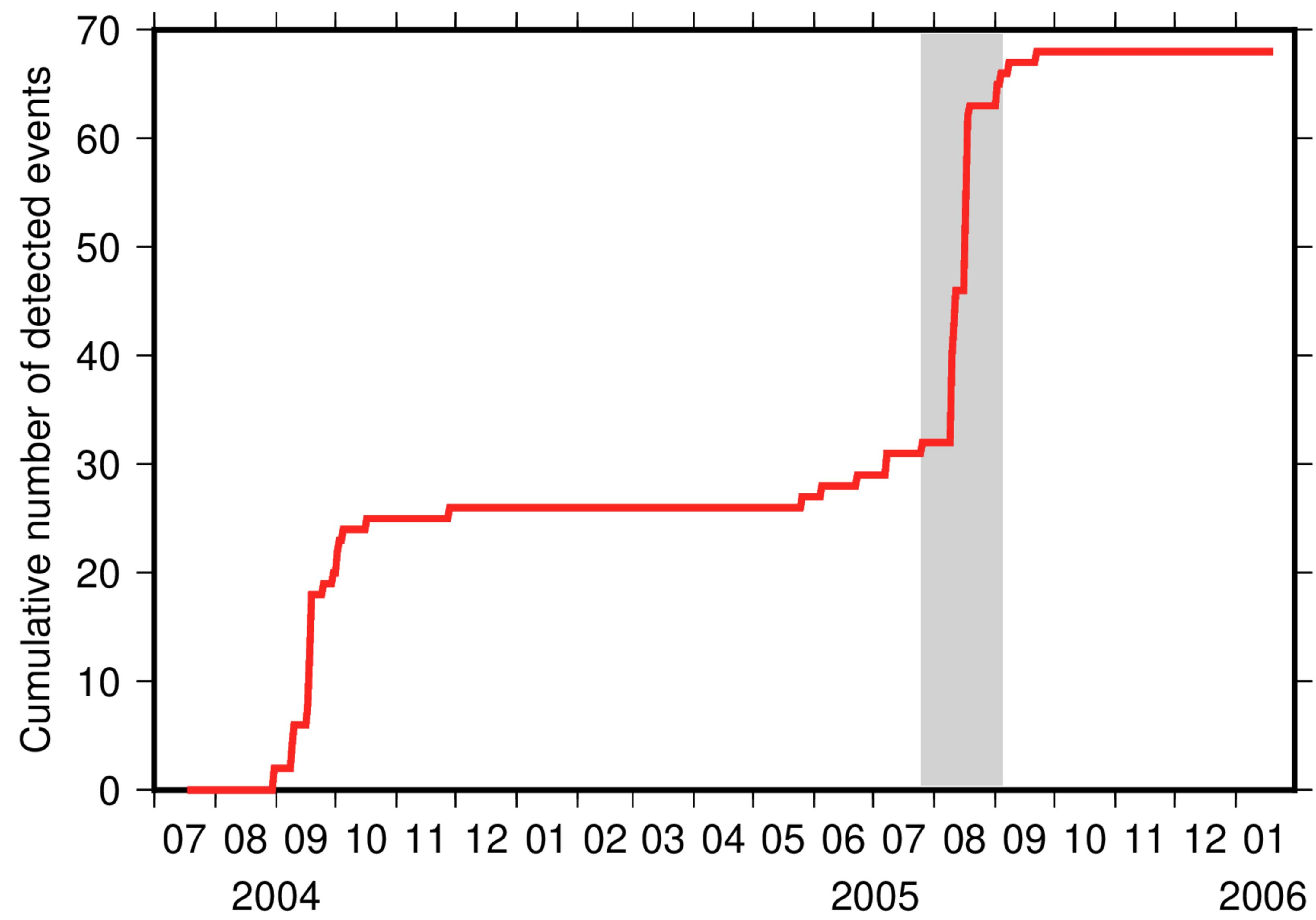


Figure 4.

(a)



(b)

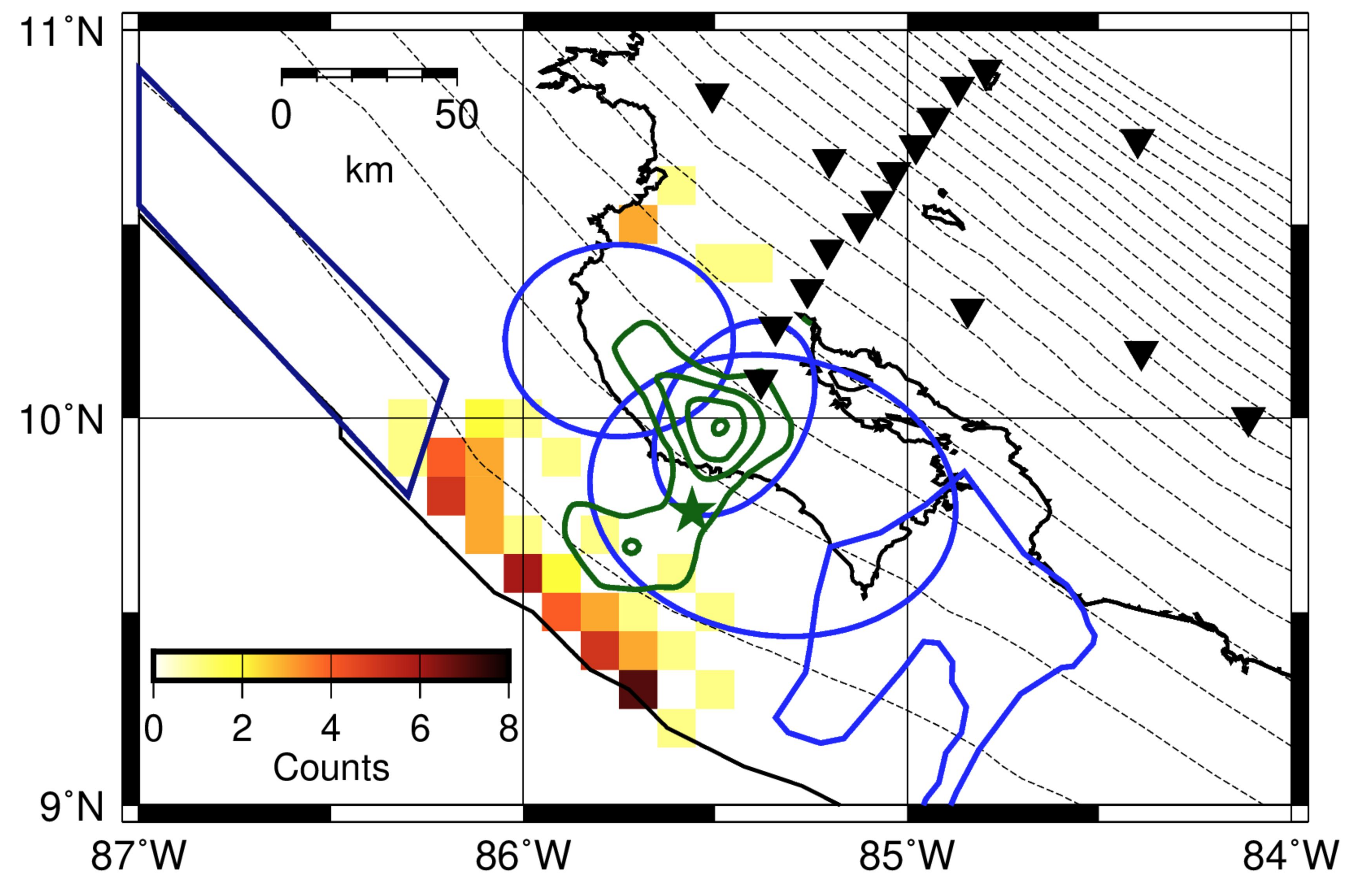
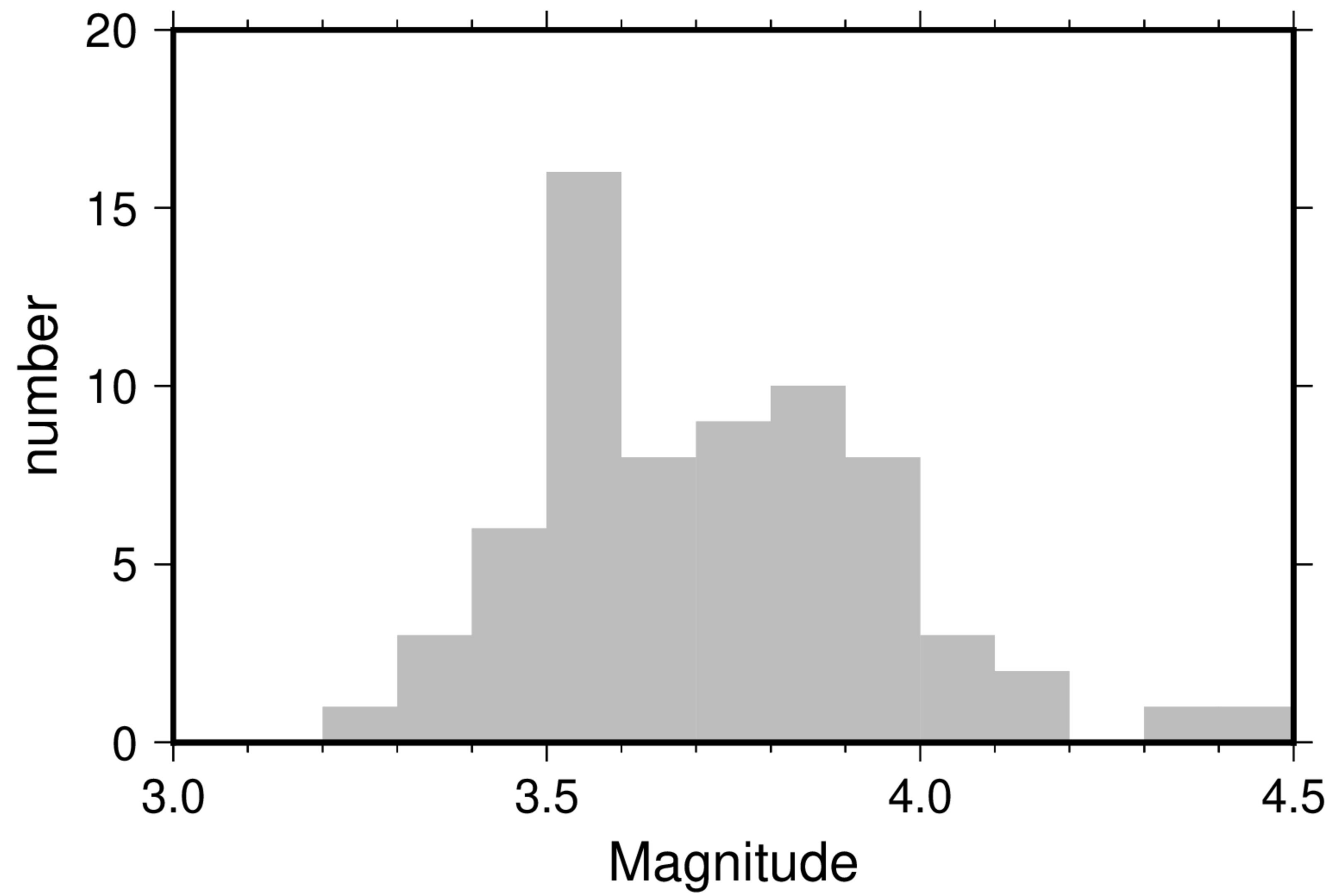
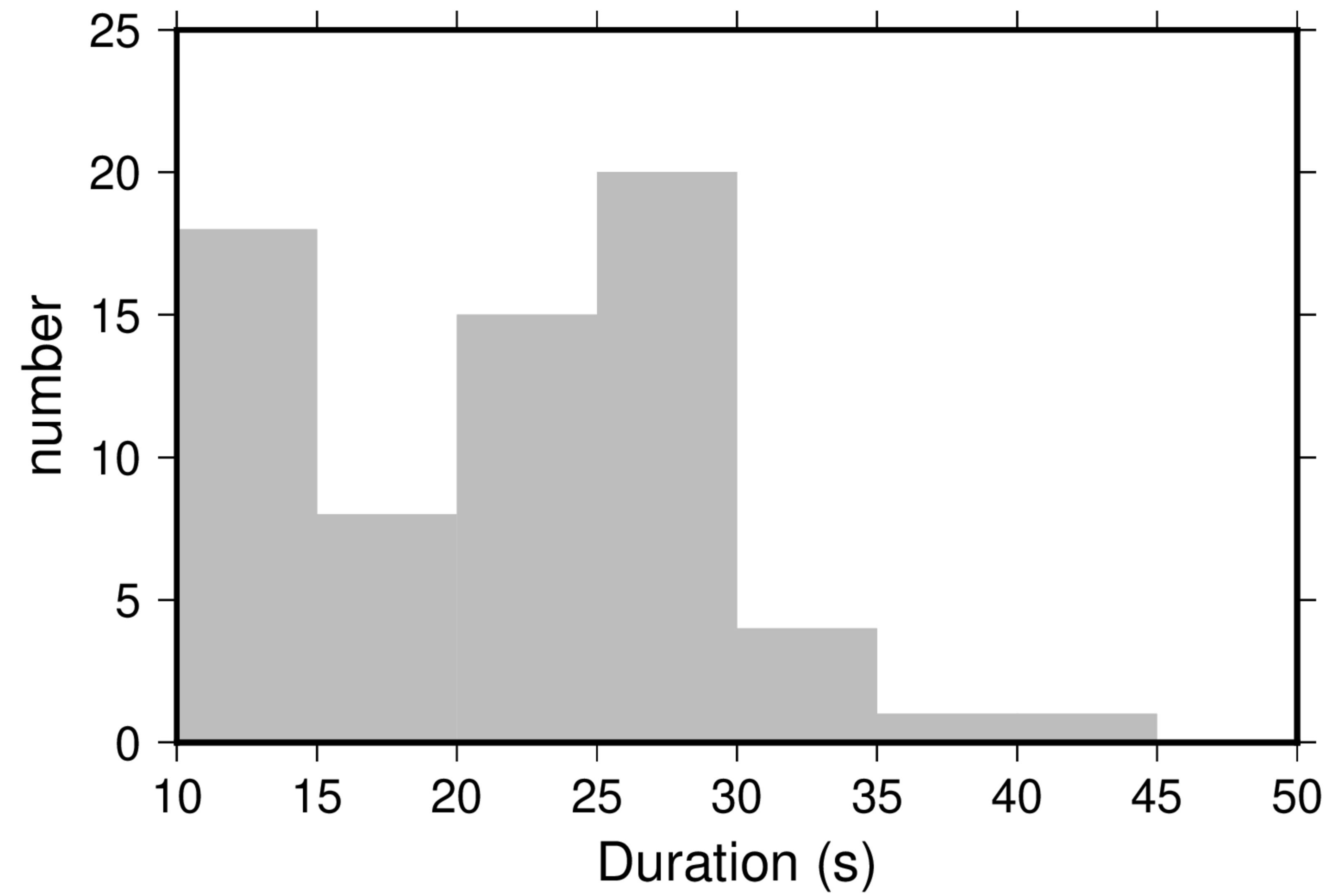


Figure 5.

(a)



(b)



(c)

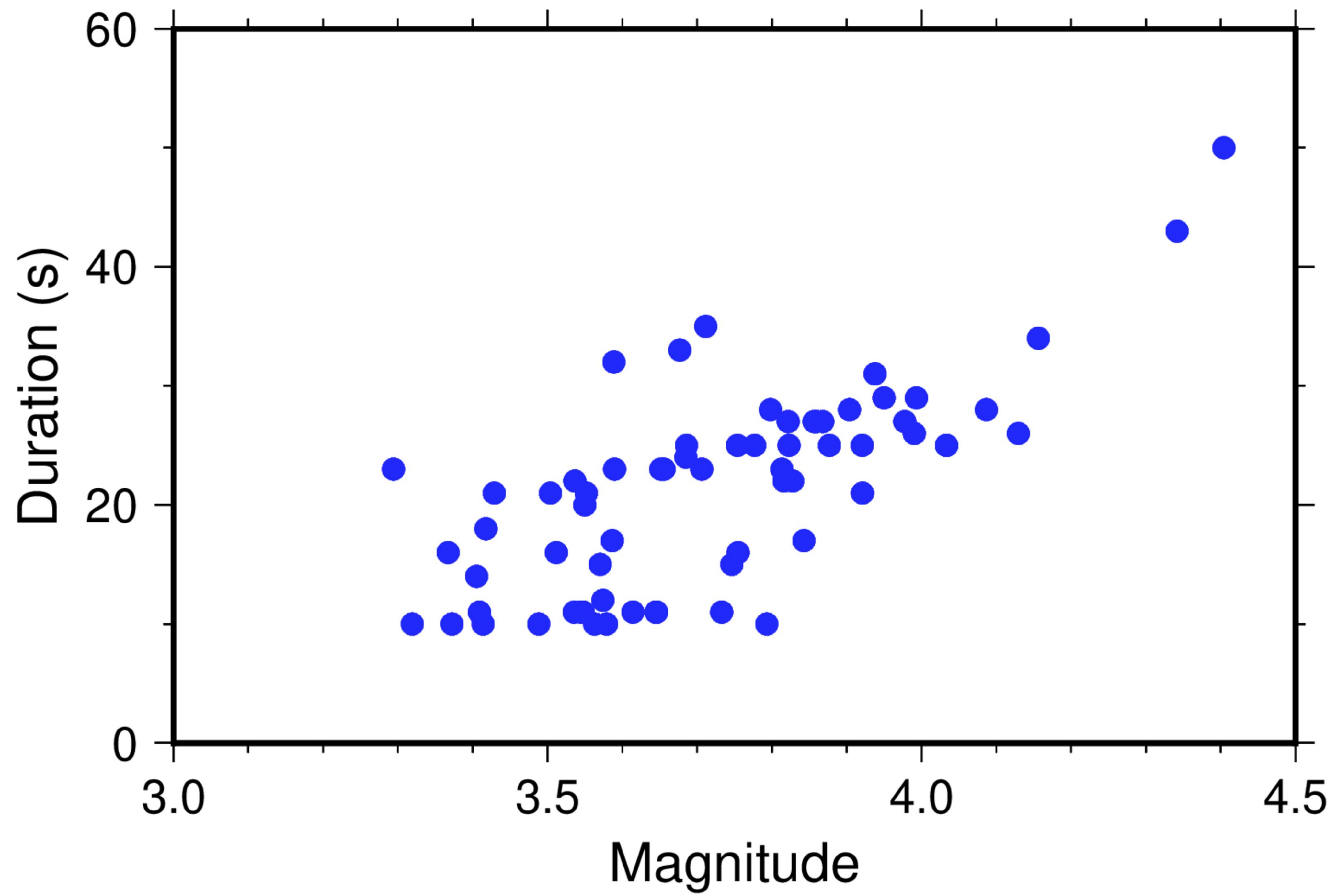
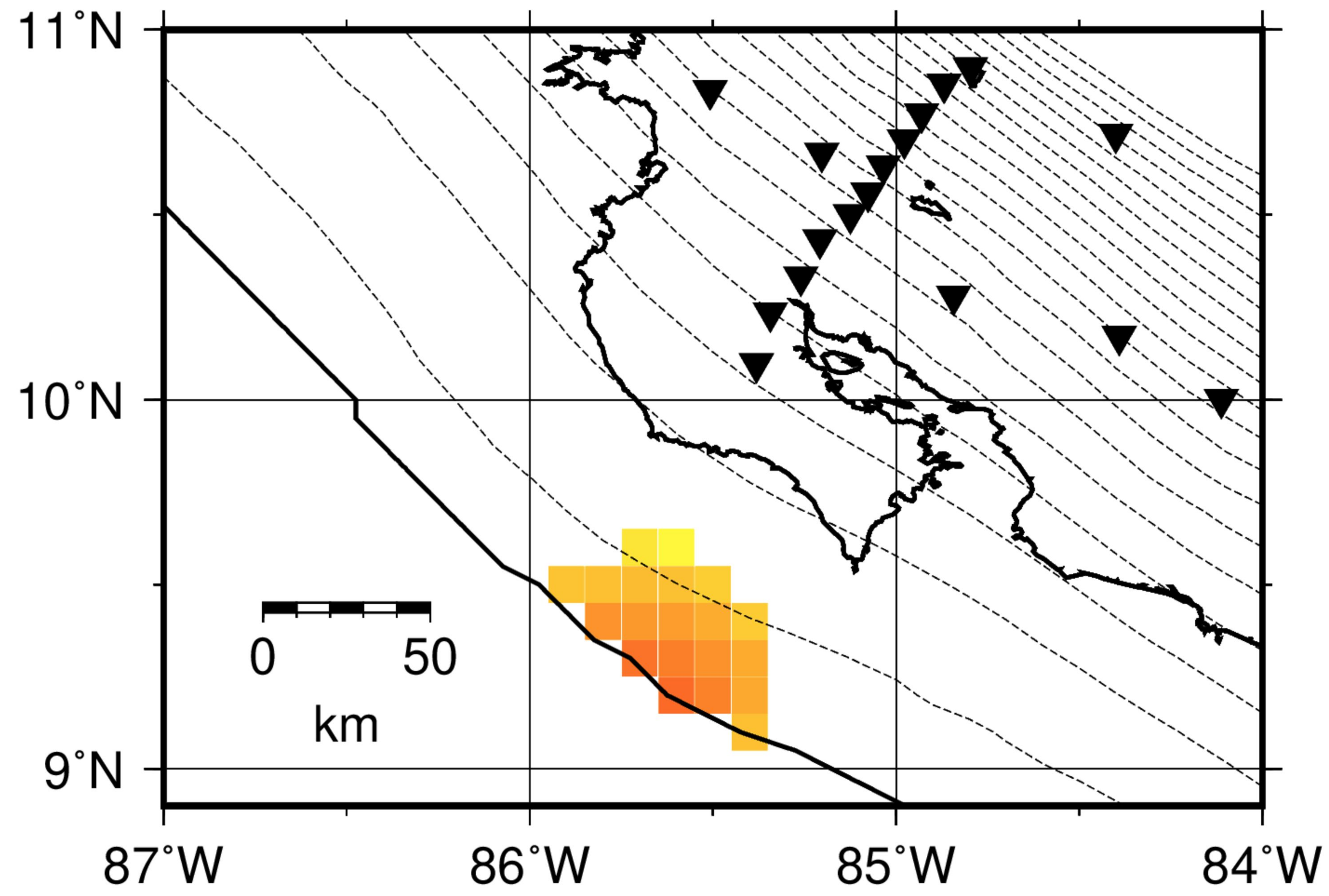
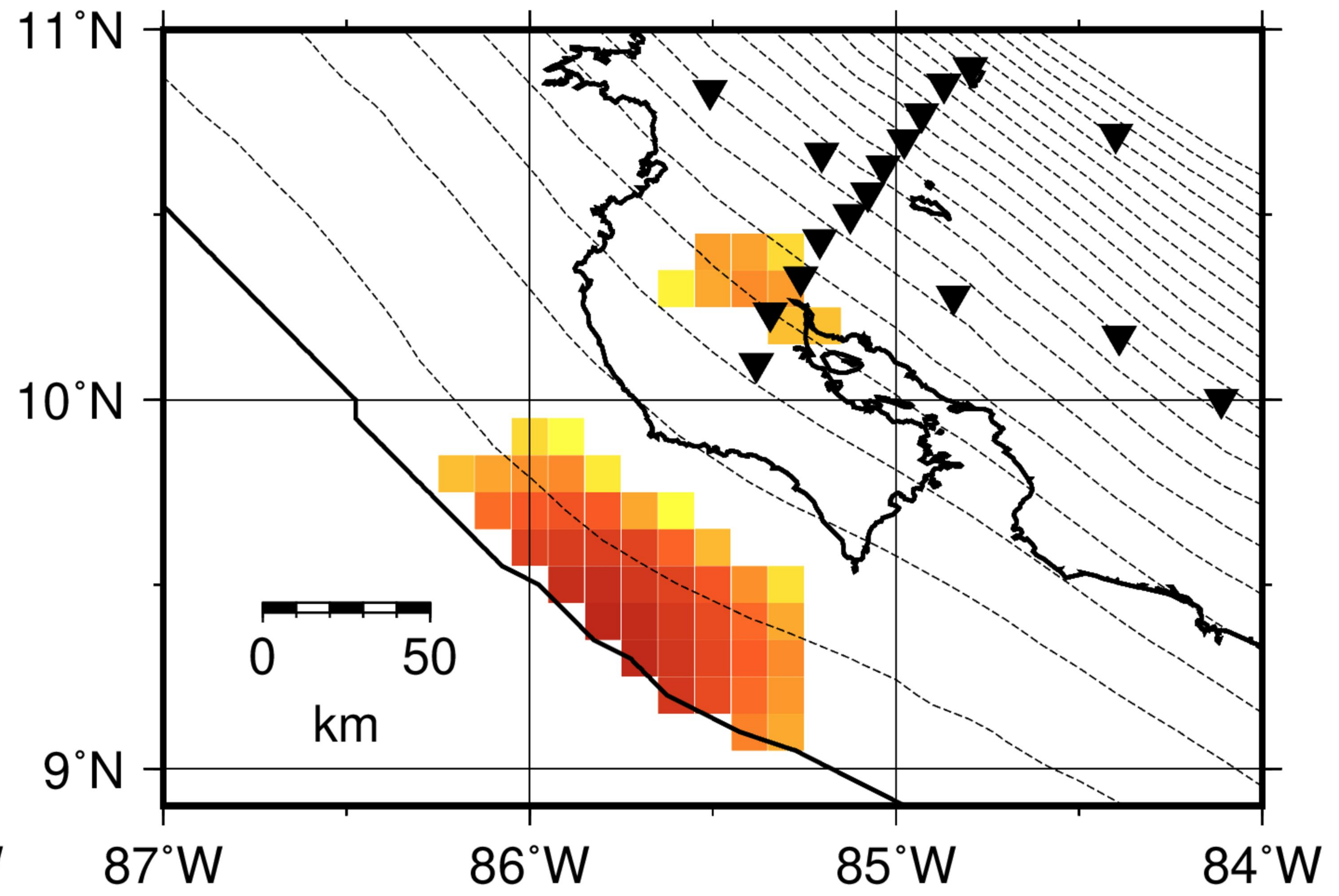


Figure 6.

(a) 2005/08/10 12:48:50



(b) 2005/08/10 03:53:47



(c) 2005/08/18 00:40:43

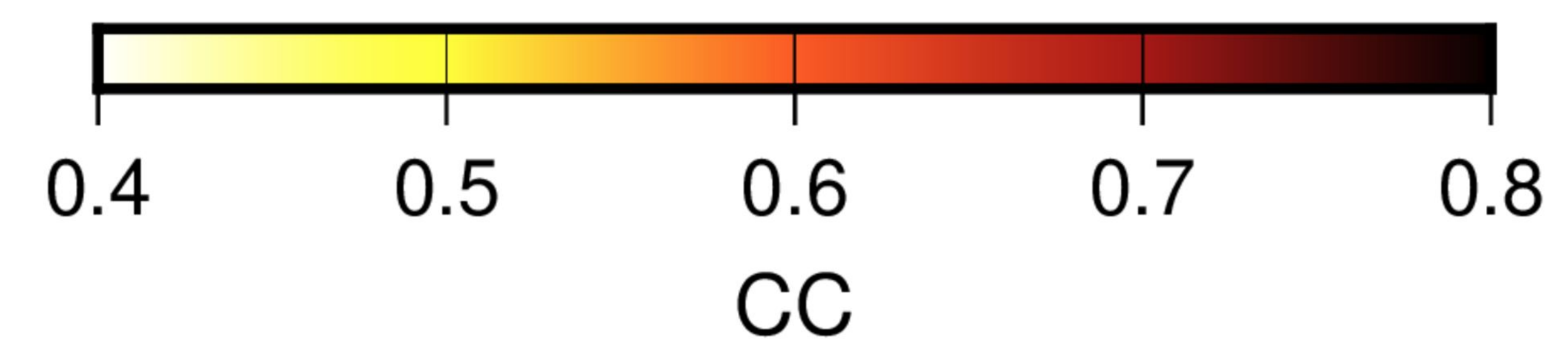
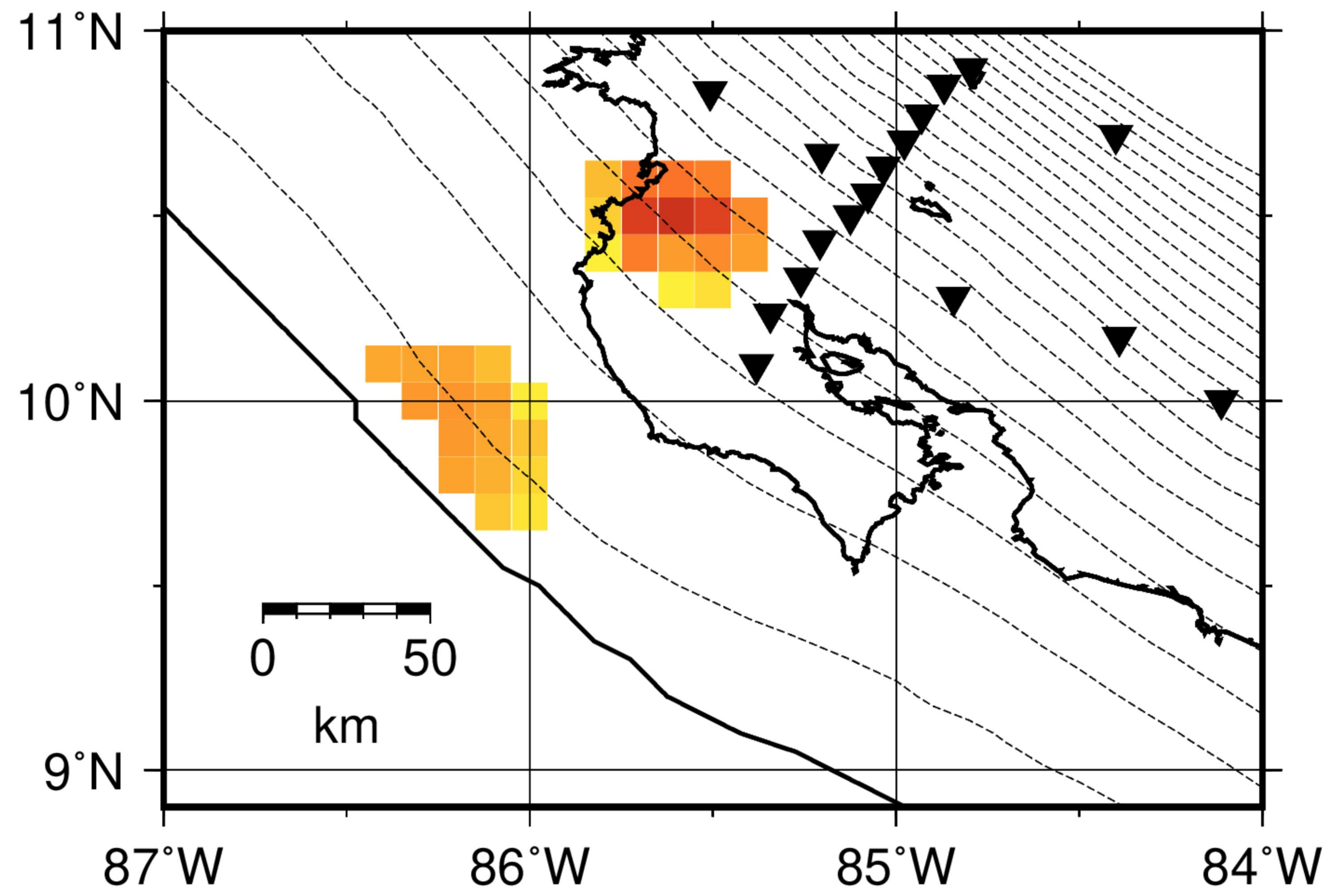


Figure 7.

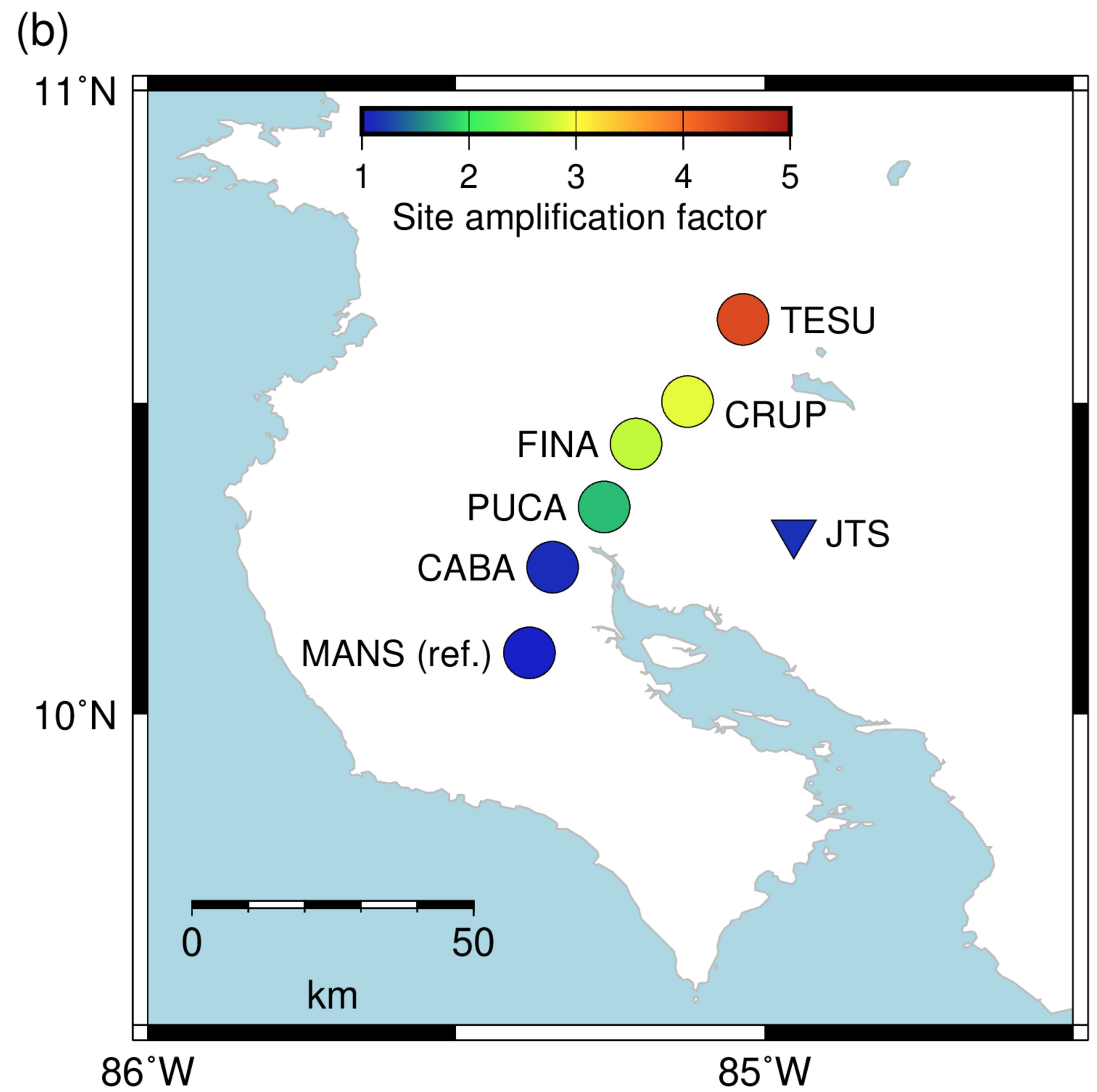
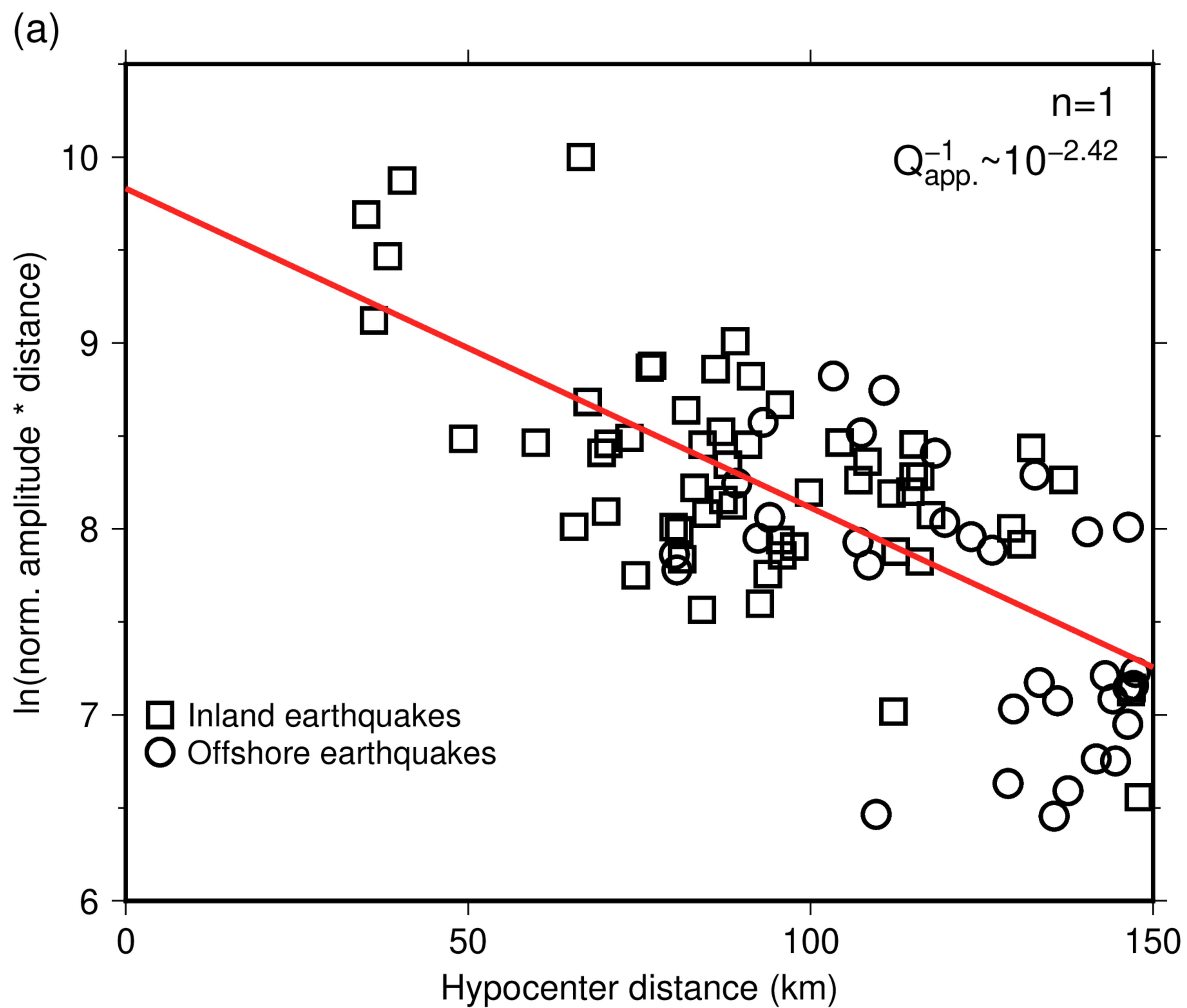


Figure 8.

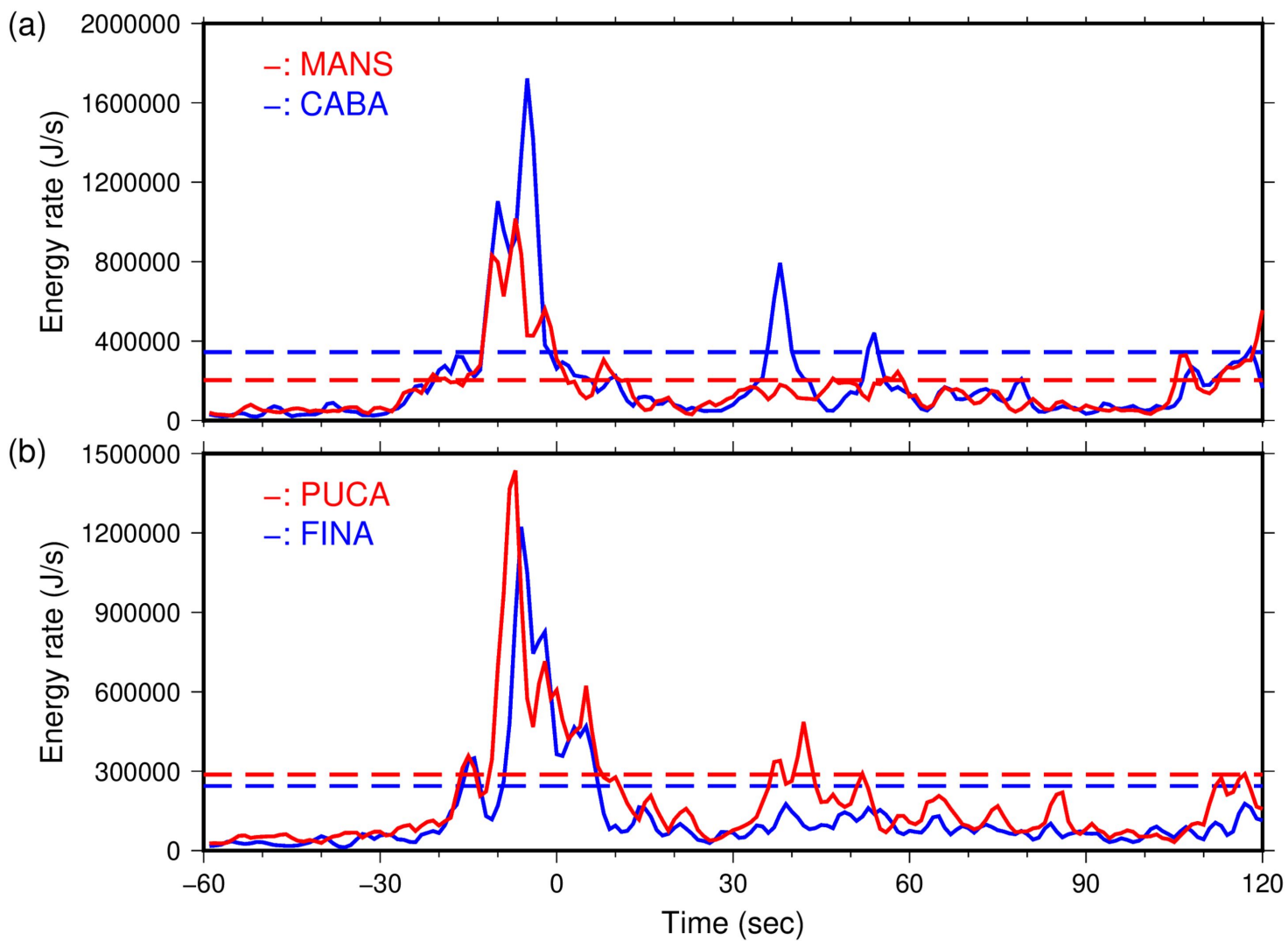


Figure 9.

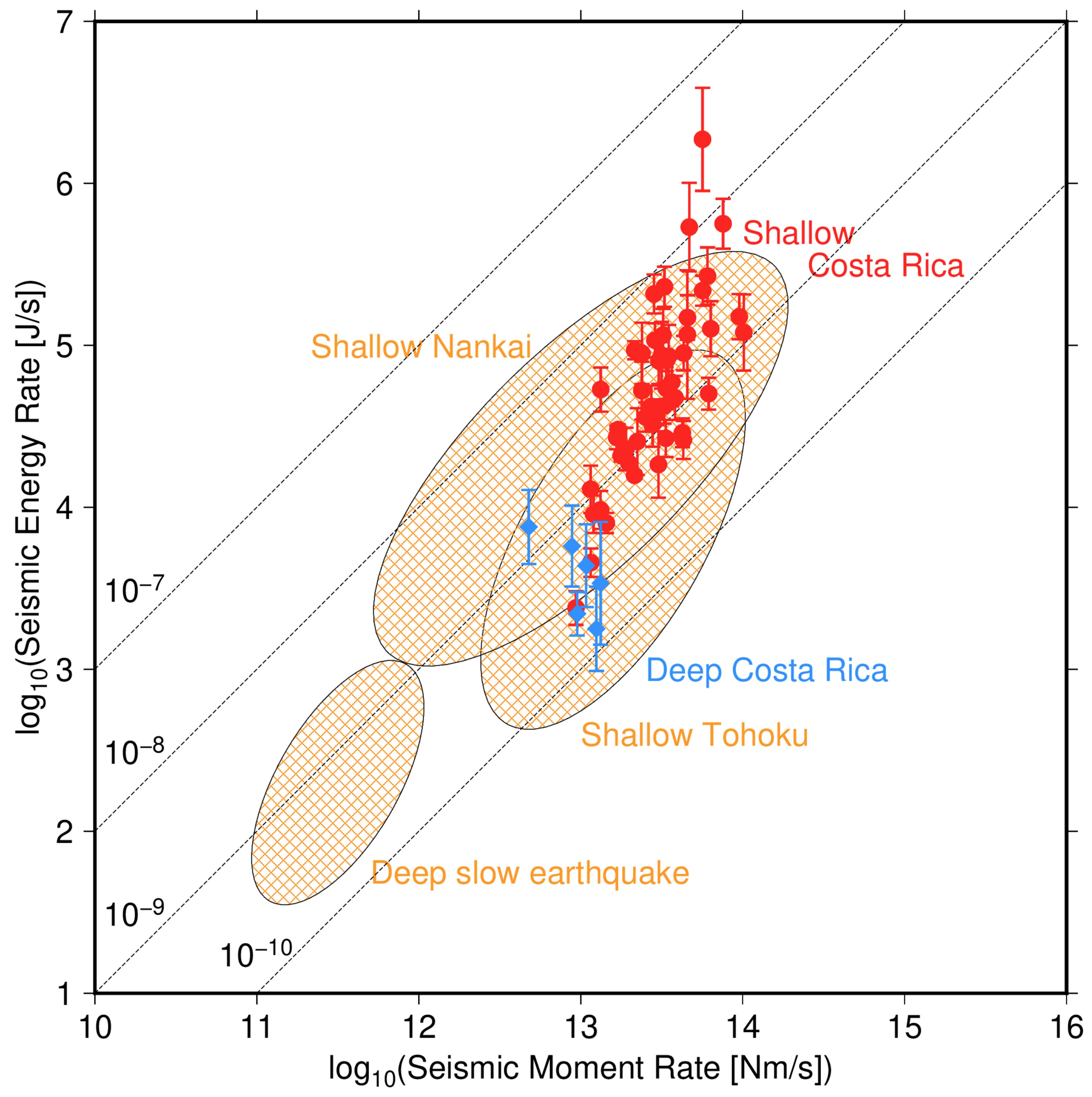


Figure 10.

